0 0 0 0 4 3 0 0 9 3 8

LBL-3636
c.1

AN EXPERIMENTAL STUDY OF THE REACTION $p + d \rightarrow {}^3He + \pi^0$ IN THE $\Delta(1236)$ RESONANCE REGION

Donald H. Fredrickson
(Ph.D. thesis)

RECEIVED
BERKELEY LABORATORY
AUG 8 1975
LIBRARY AND
DOCUMENTS SECTION

August 1974

Prepared for the U.S. Energy Research and
Development Administration under Contract W-7405-ENG-48

For Reference

Not to be taken from this room

LAWRENCE BERKELEY LABORATORY
UNIVERSITY OF CALIFORNIA
BERKELEY

LBL-3636
c.1

DISCLAIMER

This document was prepared as an account of work sponsored by the United States Government. While this document is believed to contain correct information, neither the United States Government nor any agency thereof, nor the Regents of the University of California, nor any of their employees, makes any warranty, express or implied, or assumes any legal responsibility for the accuracy, completeness, or usefulness of any information, apparatus, product, or process disclosed, or represents that its use would not infringe privately owned rights. Reference herein to any specific commercial product, process, or service by its trade name, trademark, manufacturer, or otherwise, does not necessarily constitute or imply its endorsement, recommendation, or favoring by the United States Government or any agency thereof, or the Regents of the University of California. The views and opinions of authors expressed herein do not necessarily state or reflect those of the United States Government or any agency thereof or the Regents of the University of California.

0 0 0 4 3 0 0 9 3 9

TABLE OF CONTENTS

I. Introduction

A. Objectives 1

B. Pion Production in Bound State Reactions 2

C. Isotopic Spin Invariance 9

1. A Brief History of the Development of the Principles of Isotopic Spin Invariance

2. Experimental Tests of Isotopic Spin Invariance

II. Experimental Apparatus

A. General Description 13

B. Beam 16

1. Beam Transport

2. Beam Dispersion

3. Beam Divergence

4. Beam Energy

5. Beam Intensity

6. Beam Steering

C. Target 22

D. Helium Spectrometer 27

1. Magnetostrictive Wire Spark Chambers

2. Energy-Loss Counter

3. Helium Energy Counter

4. Anti-Coincidence Counter

E. Photon Detector 29

F. Running Conditions 33

III. Data Analysis

A. General 35

B. Helium Trajectory 38

C. Helium Energy 40

D. Geometric Acceptance 42

E. Least-Squares Kinematic Fitting 44

F. Efficiencies 48

1. General

2. Spark Chamber Efficiency

3. Counting Efficiency

G. Background 51

H. Cross-Section Calculation 53

I. Errors and Corrections 57

1. ^{3}He Break-up

2. Efficiency of the Goodness of Fit Cut

3. Target Thickness

4. Target Empty

IV. Experimental Results 61

0 0 0 4 3 0 0 9 4 0

V. Discussion and Conclusions

A. Models for Pion Production 65

B. Isotopic Spin 74

Acknowledgements 77

Appendices

A. Beam Energy Calibration 78

B. Ionization Chamber Calibration 81

C. Least-Squares Kinematic Fitting 86

D. Electromagnetic Corrections to Isospin Invariance ... 89

References 91

0 0 0 4 3 0 0 9 4 1

V. Discussion and Conclusions

A. Models for Pion Production 65

B. Isotopic Spin 74

Acknowledgements 77

Appendices

A. Beam Energy Calibration 78

B. Ionization Chamber Calibration 81

C. Least-Squares Kinematic Fitting 86

D. Electromagnetic Corrections to Isospin Invariance ... 89

References 91

0 0 0 0 4 3 0 0 9 4 2

Abstract

The differential cross-section of the reaction $p+d \rightarrow {}^3He+\pi^0$ was measured at an incident proton energy of 462 MeV for ^3He c.m. angles between 50 and 130°. Limited angular distributions were also obtained at 377 and 576 MeV. The ^3He particle momentum was measured by using wire spark chambers in conjunction with a total energy absorption scintillation counter. A decay photon from the π^0 was detected in a lead glass Cerenkov counter. The results are discussed in terms of a two-nucleon model and a OPE model of the reaction. The cross-section at 462 MeV is also compared with that of its isospin conjugate reaction, $p+d \rightarrow {}^3H+\pi^+$, and agreement with the principle of isospin invariance is satisfactory, except at small pion angles.

I. INTRODUCTION

A. Objectives

The reaction

$$p + d \rightarrow {}^3He + \pi^0 \qquad (1)$$

was studied experimentally at proton energies of 377, 462, and 576 MeV. This study was part of a more comprehensive investigation of radiative final states in ^3He formation from proton-deuteron interactions. The primary objective of the study was to measure the differential cross-section for the reaction

$$p + d \rightarrow {}^3He + \gamma \qquad (2)$$

which constitutes one part of a reciprocity test of time-reversal invariance in the electromagnetic interaction.[1] Since the cross-section for reaction (1) is larger by a factor of 20 than that for reaction (2), and furthermore since the kinematics of the two reactions are very similar in this energy region, a thorough understanding of reaction (1) is required for an accurate measurement of the cross section for reaction (2).

Reaction (1) is also interesting in its own right, specifically from the point of view of pion production in bound state interactions and with respect to isotopic spin (isospin) invariance in strong interactions. The production of mono-energetic pions in bound state interactions of protons and nuclei has been investigated for a number of targets for proton energies between 0.185 and 1.5 GeV. In addition to the experimental interest in producing pions of well-defined energy, (p,π) reactions

constitute an important method of investigating the large momentum components of nuclear wave functions. A considerable amount of effort has been spent in developing theoretical models for this process in an attempt to elucidate the pion production mechanism.

Isotopic spin invariance requires that the cross-section for the reaction

$$p + d \rightarrow {}^3H + \pi^+ \tag{3}$$

be twice that for reaction (1), i.e.,

$$\frac{d\sigma}{d\Omega}\,(pd \rightarrow {}^3H\pi^+) = 2\,\frac{d\sigma}{d\Omega}\,(pd \rightarrow {}^3He\,\pi^o)\ .$$

This was first pointed out by Messiah[2] and Ruderman[3] in 1952.

B. Pion Production in Bound State Reactions

Pion production on nuclei in which the final state consists of a bound nucleus involves momentum transfers on the order of 600 MeV/c $\equiv$ $(0.33\ \text{fm})^{-1}$. By nuclear standards this is a very high momentum, and such (p,π) reactions should be sensitive to short-range or high-momentum properties of the nuclear wave function.

The pion production mechanism in these reactions is only well known for the case in which the target nucleus is simply a nucleon. The reaction $p(p,\pi^+)d$ has been studied extensively[4] and is clearly dominated by the (3,3) resonance near 600 MeV (see fig. 1). For more complex targets Ruderman[5] suggested that a similar mechanism should prevail when sufficient energy is available in the c.m. system to excite one of the nucleons to the (3,3) resonance state. This two-nucleon process occurs

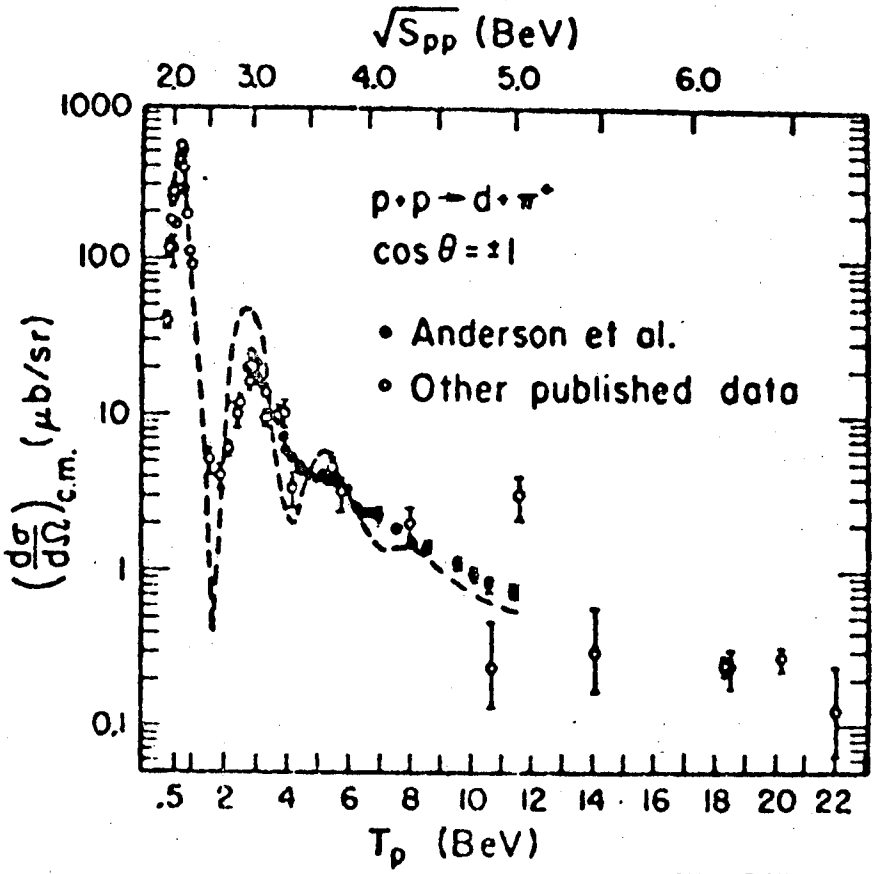

XBL 747-1171

Fig. 1 The center-of-mass forward ($\cos\Theta = \pm 1$) differential cross-section for $p + p \longrightarrow d + \pi^+$ as a function of incident proton lab. energy, and of the total c.m. energy. The figure is from Barry (Ref.45).

when the incident nucleon interacts with a nucleon within the target nucleus, causing a pion to be emitted with the incident nucleon being captured by the target nucleus. For an example of this mechanism see fig. 2(b). Ingram et al.[6] have made a calculation based on this process which relates the reaction $A(p,\pi^+)A+1$ to the elementary reaction $p(p,\pi^+)d$. For low energy pion production a single-nucleon mechanism is thought to be more appropriate.[7] In this case the incident nucleon emits a pion before the nucleon is captured by the target nucleus. Examples of this type of process are shown in fig. 4. Since the momentum transfer required in a single-nucleon process is $A/(A-1)$ times greater than that required in a two-nucleon process, the latter should be the more likely mechanism in the case of pion production off light nuclei at medium energy.

The reactions $pd \rightarrow \begin{cases} {}^3He\,\pi^0 \\ {}^3H\,\pi^+ \end{cases}$, above T_p=300 MeV exemplify such a case. The measurement of the differential cross-section for either of these reactions provides a test of the validity of the two-nucleon approximation. If this approximation is born out by the general shape of the cross-section, then specific information concerning the ^3H and ^3He wave functions at small distances can be extracted.

Ruderman[3] first described the reaction $d(p,\pi^+)t$ in terms of the reaction $p(p,\pi^+)d$ using the two-nucleon approximation. In his model the incoming proton is presumed to collide with the proton in the deuteron target, producing a pion together with a di-nucleon in the iso-singlet state. Provided the velocity vectors are favorably matched, the di-nucleon can then pick up the "spectator" neutron from the original deuteron to form the final state ^3H. In such a case the momentum transfer involved is

0 0 0 4 3 0 0 9 4 5

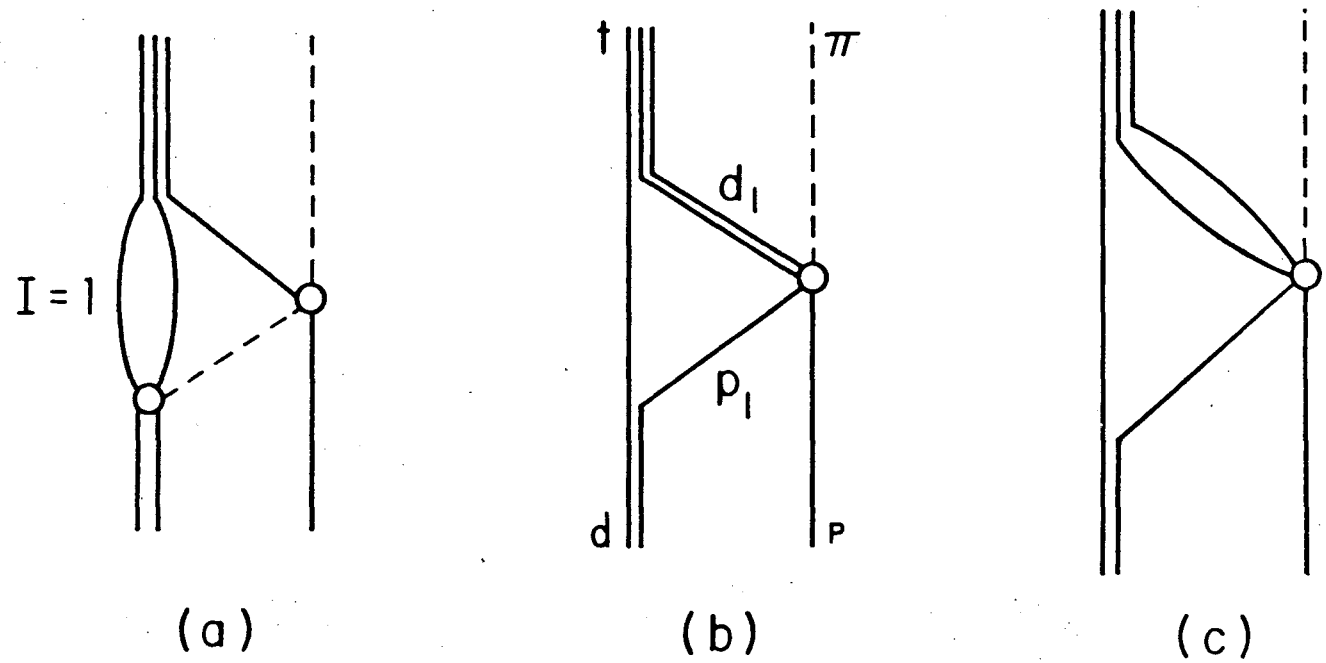

XBL 747-3610

Fig.2 Feynman graphs important for forward pion production in the reaction $p+d \rightarrow t+\pi^+$: (a) One-Pion-Exchange (OPE) process; (b) and (c) two-nucleon process.

$$\vec{\Delta} = \tfrac{1}{2}\vec{d} - \tfrac{1}{3}\vec{t} \ ,$$

where the vectors represent the c.m. momenta. On the basis of such a description, the cross-section is expected to be proportional to a deuteron-triton form factor and to the $p(p,\pi^+)d$ cross-section. Bludman[8] applied this model to the data of Frank et al.[9] at T_p=340 MeV and obtained good agreement using a deuteron wave function with a hard core as an adjustable parameter. Ingram et al.[6], whose formulation differs from Ruderman's principally in the more complicated prescription for evaluating the cross-section for $p(p,\pi^+)d$ and also in kinematical factors, obtained reasonably good quantitative agreement with the energy distribution of the forward cross-section except for the overall normalization. This depended on the particular deuteron and tritium wave functions used, but the predictions were consistently a factor of about 2 lower than the experimental data. Agreement with the angular distribution at T_p=340 MeV was poor. Barry[10] recently generalized the two-nucleon process for the relativistic case. He also considered other processes which might contribute to this reaction. Diagrams that he considered are shown in figs. 2 and 3. Dollhopf et al.[11] applied Barry's model to their data at 470 MeV and 590 MeV. Trying several different deuteron and tritium wave functions, they obtained only qualitative agreement. A serious shortcoming of the model appears to be its inability to reproduce the peak at backward π angles in the 470 MeV data. They showed that the one-nucleon process (see fig. 4) also fails to explain this backward peak.

The reaction $d(p,\pi^0)^3He$ can also be used to test the validity of these models. In some respects the measurement of this cross-section is

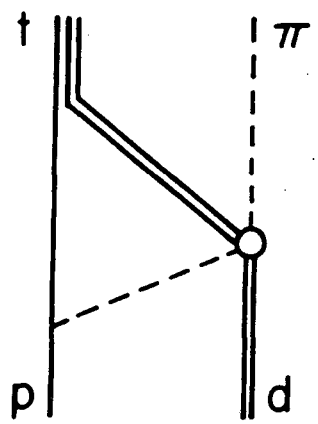

XBL 747-3608

Fig.3 One-Pion-Exchange (OPE) diagram important for backward pion production in the reaction $p+d \rightarrow t+\pi^+$.

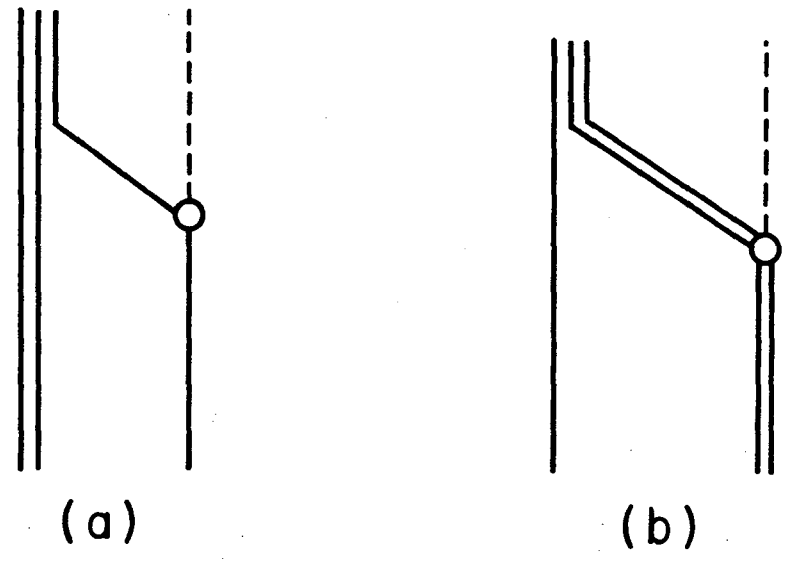

XBL 747-3609

Fig.4 Feynman graphs for the single-nucleon process in the reaction $p+d \rightarrow t+\pi^+$.

simpler than that of its isospin conjugate if both the ^{3}He and a decay photon are detected. A doubly-charged particle and a neutral in the final state constitutes a rather unique signature. In any case, it appears that the measurement of more angular distributions in the energy region between 300 and 600 MeV would help to clarify the reaction mechanism and thereby enable the extraction of some reliable information concerning the deutron, triton and ^{3}He structure. The existing data on these reactions are summarized in Table 1.

C. Isotopic Spin Invariance

1. A Brief History of the Development of the Principles of Isotopic Spin Invariance

Shortly after the discovery of the neutron in 1932, it became apparent that it had the same strong forces as the proton. Investigations of the energy levels of mirror nuclei (for example ^{7}Li and ^{7}Be) revealed striking similarities. It was found that the energy levels could be grouped into multiplets, the members of each multiplet having the same spin, parity, and nearly the same mass. This led to the postulate of charge symmetry, which states that the force between two neutrons is identical to that between two protons provided the Coulomb force is neglected.

The more general postulate of charge independence was based on experimental observations of the equality (after correcting for the Coulomb interaction) of n-p and p-p forces in free nucleon scattering in the singlet $^1S_0$ state. This principle states that at identical energies, the forces between any of the nucleon pairs (n,n), (p,n), or (p,p) depend

TABLE 1

Existing Experimental Data for the Reaction $p + d \rightarrow \begin{cases} {}^3He + \pi^0 \\ {}^3H + \pi^+ \end{cases}$

T_p (MeV) lab K.E.	θ_π (degrees)	Reaction $1 \equiv {}^3He\pi^0$ $3 \equiv {}^3H\pi^+$	Date	Reference
340	30-150	3	1954	Frank et al. (9)
670	12, 25	3	1960	Akimov et al. (41)
450	40	1, 3	1960	Crewe et al. (18)
591	37, 113, 128	1, 3	1960	Harting et al. (19)
562-750**	24, 111-131	1, 3	1963	Booth (42)
325*	0, 150-180	1	1964	Chapman et al. (40)
1515	180	1	1967	Melissinos et al. (43)
760* 1050* 760-1050*	25-180 0-180 180	1	1973	Banaigs et al. (39)
470 590	30-160 90-160	1	1973	Dollhopf et al. (11)

* Deuteron used as the projectile. The number given is the equivalent proton energy.

** Data points at isolated energies and angles within the indicated ranges.

only on the total angular momentum and parity of the pair, and not on their charge state. In 1936 Cassen and Condon[12] showed that the principle of charge independence could be elegantly expressed by means of the concept of isotopic spin or simply isospin. Isospin is analogous to angular momentum but is linked to the charge states of the system in question. It uses the same mathematical formalism that was developed for angular momentum. The nucleon is endowed with another degree of freedom besides the ordinary ones of coordinate and spin, and the corresponding internal variable is called isospin. In this formalism, the neutron and proton are manifestations of the same particle, the nucleon. Since this system is a doublet, it was natural to pursue the analogy with angular momentum and assign an isospin "vector" of value 1/2 to the (n,p) system. The space in which this orientation is described is not physically realizable but is called "isospin space". The neutron and proton are manifestations of the two different orientations of the nucleon in this space.

The association of pi-mesons with charge independence was first made by Kemmer[13] in 1938. The two charged pi-mesons have identical mass and the neutral pi-meson is only 3% less massive. Furthermore they all have the same spin and parity. Therefore it was natural to associate these three mesons with another isospin multiplet, and isospin triplet. This last step led to a principle even more general than charge independence, to the principle of isospin invariance. The postulate of isospin invariance states that the reaction amplitude depends only on the value of the isospin, I, and not on I_3, the component of the isospin associated

with the charge state. In the case of nucleon-nucleon interactions, charge independence and isospin invariance are equivalent as a consequence of the nucleon having an isospin of 1/2.

2. Experimental Tests of Isotopic Spin Invariance

Isospin invariance manifests itself in the energy level structure of light nuclei, in selection rules among possible nuclear reactions, and in ratios of cross-sections for reactions involving various members of a given isospin multiplet. The energy levels of light nuclei have been grouped into definite isospin multiplets, differing (aside from small discrepancies in mass) only in the value of the charge or I_3. The excited states of the mirror nuclei ^{7}Li and ^{7}Be afford a good example of tests of isospin invariance in bound states. These levels are equal to within 2 - 4%.[14] Isospin tests in bound state systems are difficult because of the problem of correcting for Coulomb interactions.

The reaction $d+d \rightarrow \alpha+\pi^0$ is an example of the manifestation of isospin invariance as a selection rule. The π^0 has isospin 1, whereas the other particles have zero isospin. Therefore the reaction is forbidden. An experimental upper limit for the cross-section has been measured,[15] and a calculation[16] based on the results indicates that isospin is conserved to within at least 6.5%.

For elastic scattering in the (π,d) system, the cross-section should be independent of the pion charge. Measurements[14,17] for π^+ and π^- scattering indicate that the cross-sections are equal to within 0.75%. These reactions, however, only test invariance with respect to the I_3 component but not to total isospin, I.

The $pd \rightarrow \begin{cases} {}^3He\,\pi^0 \\ {}^3H\pi^+ \end{cases}$ system, however, affords a convenient check of both I and I_3. Isospin invariance has been tested in this system at isolated energies and angles. As stated previously, isospin invariance requires that the cross-sections have the ratio

$$\frac{\sigma({}^3H)}{\sigma({}^3He)} = 2 \ .$$

Crewe et al.[18] found agreement to within an accuracy of 15% at T_p=450 MeV at an angle of 140° for the heavy particle. Harting et al.[19] found agreement to within an accuracy of 5% for T_p=591 MeV at angles of 52, 67, and 143° for the heavy particle. This test involves rather large corrections[20] (approximately 6% and angle-dependent) due to EM effects.

With the results of the current experiment this test can be extended to a large angular region at 462 MeV.

II. Experimental Apparatus

A. General Description

A floor plan of the experiment is shown in fig. 5. The external proton beam of the Lawrence Berkeley Laboratory 184-inch Synchrocyclotron was passed through a degrader and sent through a spectrometer system, which used a set of bending magnets to disperse the beam, a slit to select the desired momenta, and a second set of bending magnets to recombine the selected momenta. At the entrance to the experimental area, the degraded proton beam passed through the first of three ion chambers before entering the vacuum chamber leading to the liquid deuterium target.

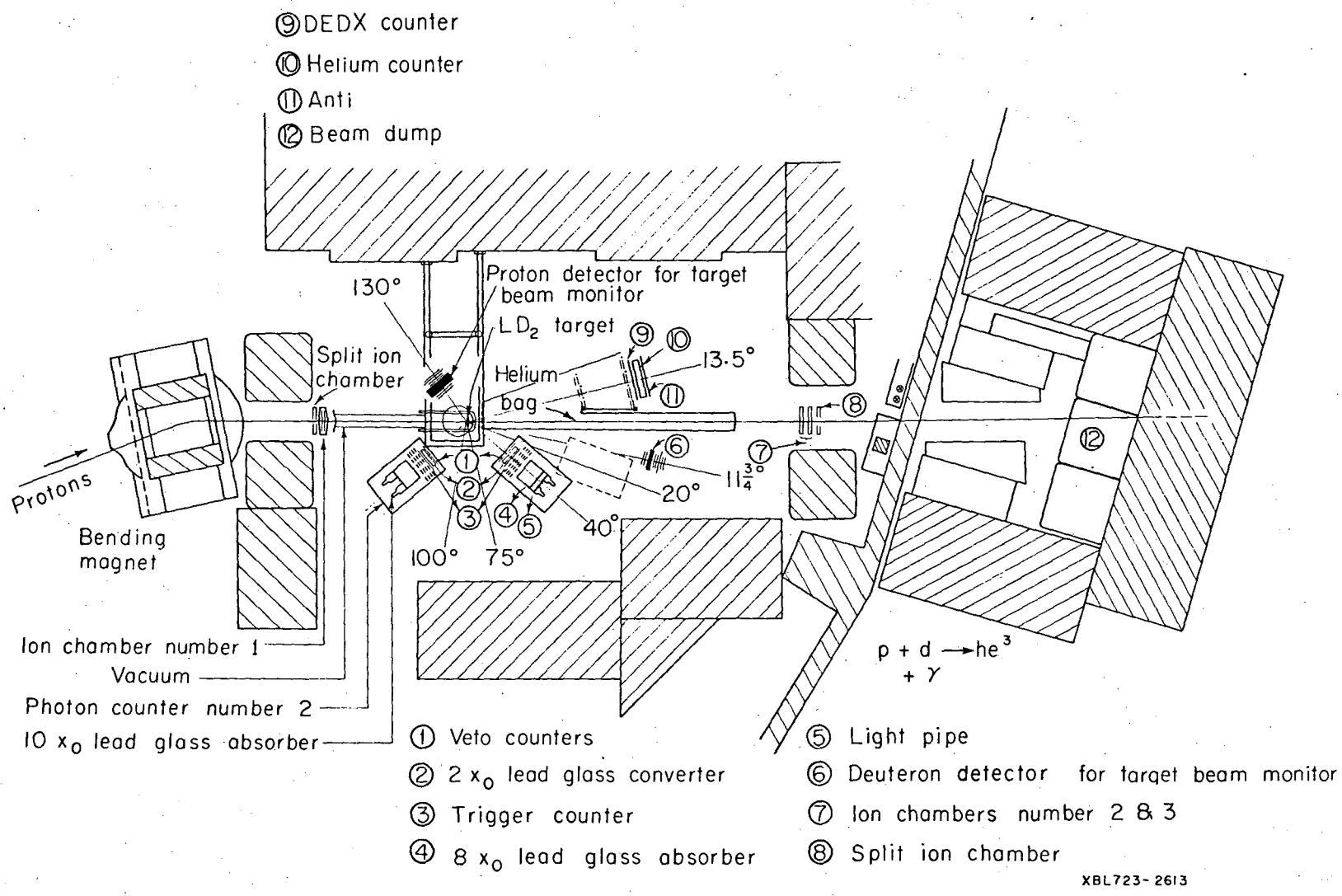

Fig.5 Plan view of the experimental apparatus.

The trajectory of the ^{3}He particle was determined by two wire spark chambers, and particle energy was measured in a large scintillation counter. An energy-loss counter (DEDX) was used before the energy counter to select doubly charged particles, and a veto counter behind the energy counter rejected events in which charged particles passed through the energy counter.

A photon from the decaying π^o was detected by means of a lead glass Cerenkov counter. A veto counter was used to reject charged particles. In the Cerenkov detector the photon was converted by a lead glass slab, and the resulting charged particles were detected by a scintillation counter. Spatial information was obtained from spark chambers which followed the scintillation counter and which preceded a large block of lead glass. The lead glass produced and contained the ensuing shower and gave a rough measurement of the photon energy.

The product of beam intensity and target thickness was monitored by measuring the elastic pd scattering rate using two scintillator telescopes in coincidence. A pair of ion chambers at the rear of the experimental area monitored beam intensity. Beam steering was monitored by means of split ion chambers, one at the front and one at the rear of the experimental area.

Digitized spark coordinate information, time of flight difference between the He and photon arms, and pulse heights in the He, DEDX, and photon counters were stored on magnetic tape together with information from the various other counters.

B. Beam

1. Beam Transport

The beam transport system is shown in fig. 6. The external proton beam passes through a copper degrader and a system of defining slits (slits 1 and 2). Two bends of 23° each disperse the beam across the momentum slit (slit 3). This slit was used to select the desired momentum interval. The succeeding magnets produce an image of the momentum slit at the target. Slit 3 was used to reduce the halo of the beam spot at the target.

2. Beam Dispersion.

The momentum dispersion across the target was expected to be 0.45% per inch. This dispersion was the result of incomplete momentum recombination in the horizontal plane at the target due to geometric constraints on the beam design. The magnification was expected to be 2.2 from the momentum slit to the target.

Measurements were made of both the magnification and dispersion by narrowing the momentum slit and making three measurements with the narrow slit in different positions. The magnification was measured by means of photographic exposures to be 1.8; the momentum dispersion was measured by range measurements (see section 4 below) to be 0.36% per inch at the target. These agreements, while not excellent, are probably within the experimental uncertainties, most especially when considering survey and alignment uncertainties and errors due to the use of first-order optics.

0 0 0 4 3 0 0 9 5 1

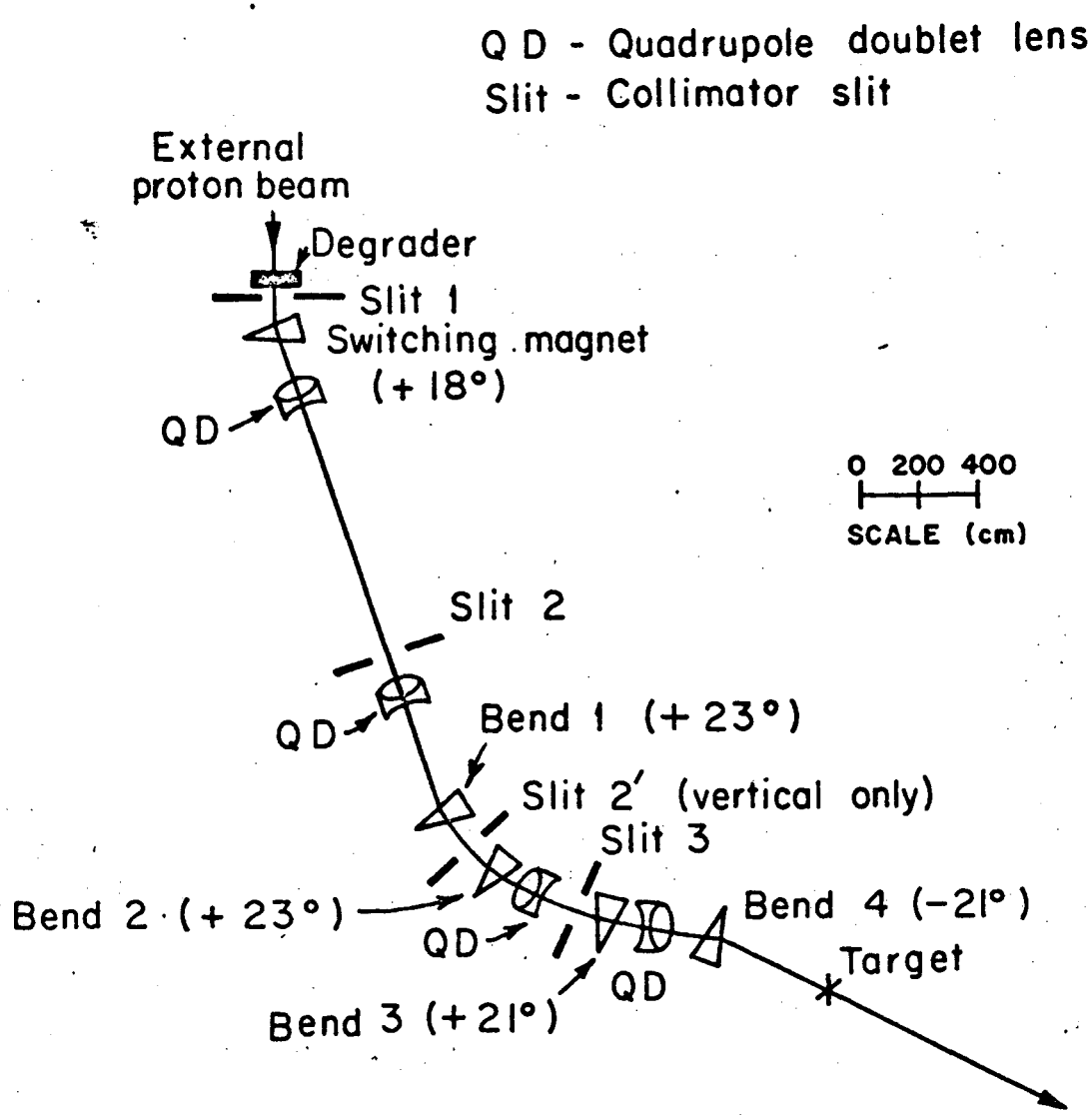

Fig.6 Schematic diagram of the beam transport system.

XBL747-3626

3. Beam Divergence

A mean horizontal divergence of about 0.5° per inch at the target was the design. Some scatter plots of run analyses reinforced this number, but there was no direct experimental verification. Vertically, the beam divergence was designed to be 0.4° per inch. In addition to this correlated divergence, there was a random beam divergence, in the horizontal and vertical planes having a standard deviation of 0.14°.

4. Beam Energy

The average proton beam energy was measured by degrading the proton energy with copper absorber and determining the Bragg peak of the protons in a helium ion chamber. The experimental set-up is shown in fig. 7. From the position and width of the Bragg peak are obtained the average proton range and standard deviation respectively. The absolute range-energy calibration is based on two experiments[21,22] which bracket the range of energies with which we are concerned. In order to assign an energy to a given event, this average beam energy is corrected by an amount based on the position of the given event with respect to the average position of all events. Beam energy determination is described in more detail in Appendix A.

5. Beam Intensity

The beam intensity was measured by a set of three helium-filled ion chambers, each with its own integrator. The integrators were periodically calibrated during the experiment with a current source (Keithley Model 201). The accuracy of the current source

0 0 0 4 3 0 0 9 5 2

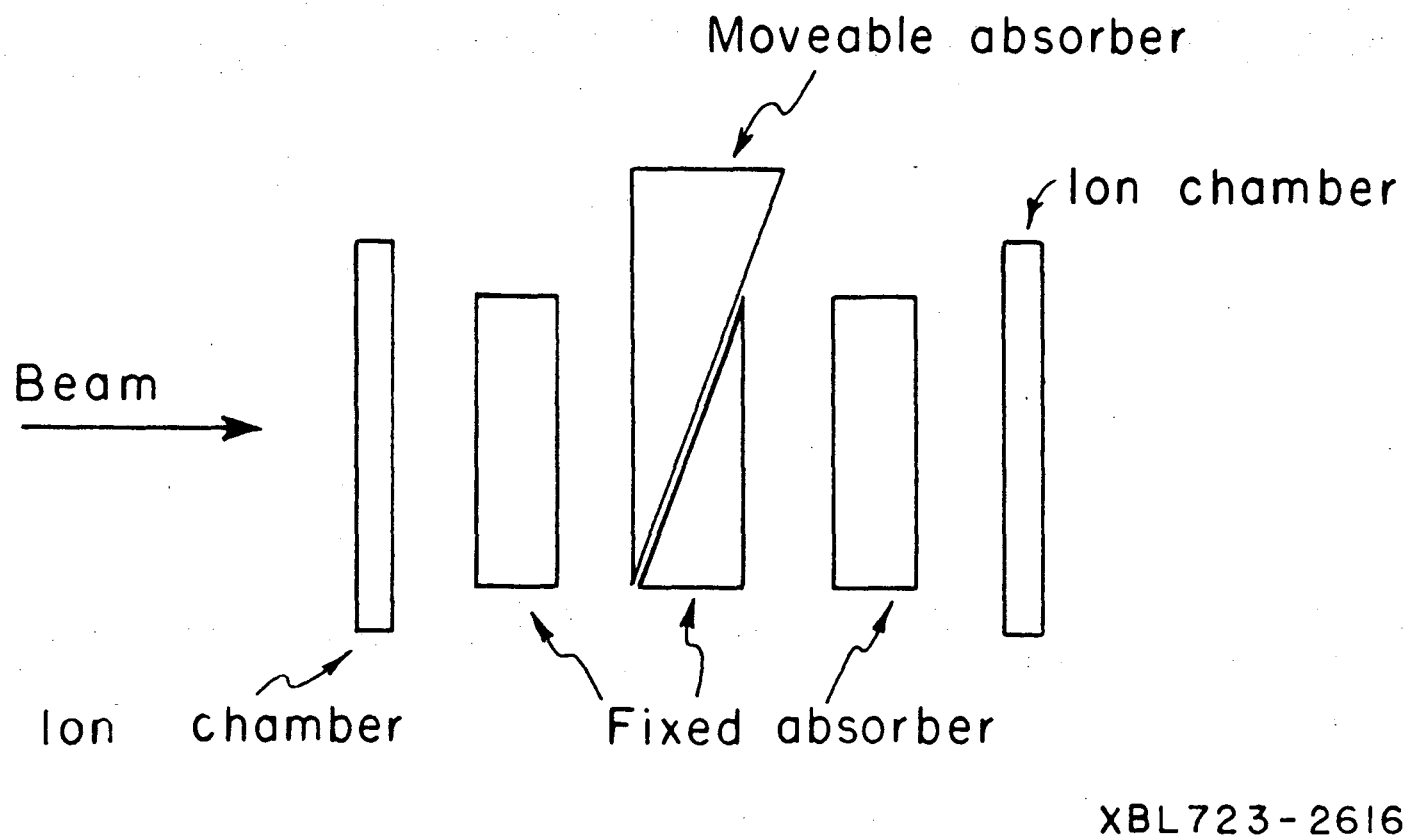

Fig.7 Schematic diagram of the apparatus for the proton energy measurement.

was not known, but the combination of current source and one of the integrators gave a measured precision for the integrator constant of 0.13% over a six month period. The three ion chambers yielded results consistent to better than 1% over the entire duration of the experiment.

A direct proton counting technique was used for the absolute calibration of the ion chambers. This technique is described briefly below and in detail in Appendix B. At a high beam rate (roughly 2×10^8 protons/sec, time averaged) the ion chamber was calibrated against the elastic proton-proton scattering rate from a CH_2 target. At this beam rate, an accurate correction for leakage current was possible. At a beam rate low enough (roughly 10^6 protons/sec, instantaneous) so that counting losses were not beyond correction, the protons were directly counted by a scintillator telescope. Concurrently, the proton-proton elastic scattering rate was measured. This provided the link between the directly counted protons of the low intensity beam and the charge collected in the ion chamber with the high intensity beam. A schematic diagram of the important parts of the apparatus used in this calibration is shown in fig. 8. The ion chamber to be calibrated was placed upstream of the direct proton counters (DPC), which consisted of three circular (12-inch diameter, 1/8-inch thick) plastic scintillators in coincidence. A four-inch thick CH_2 target downstream of the DPC was used for the proton-proton scattering. The scintillator telescopes are described in section II(c) below.

6. Beam Steering

The location and direction of the beam in the

0 0 0 4 3 0 0 9 5 3

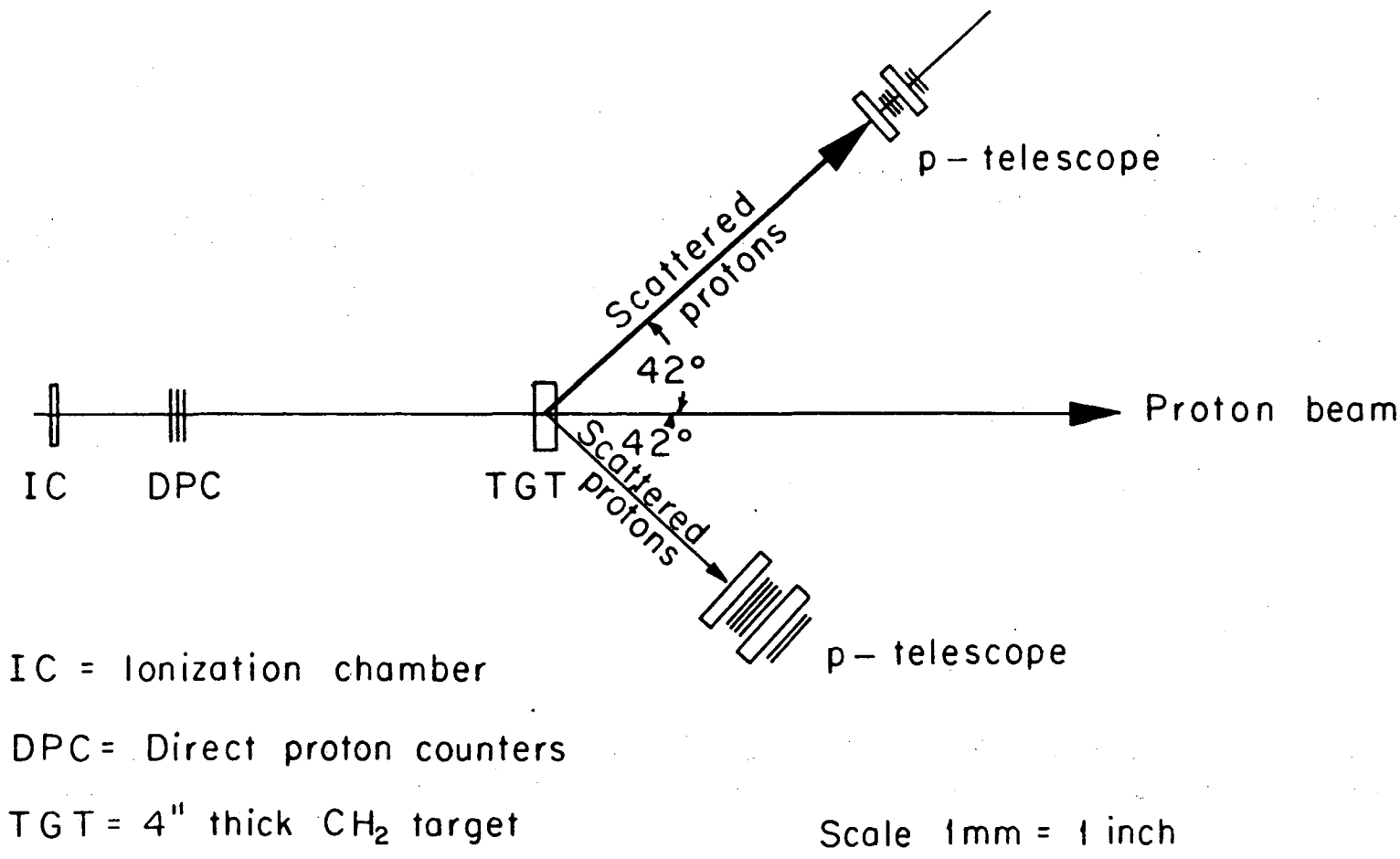

Fig.8 Schematic diagram of the apparatus for the beam intensity calibration.

horizontal plane were continuously monitored by recording the differential currents from two split ion-chambers separated by 271.5 inches (see fig. 5). Maximum beam displacement during a typical run was about 0.04°. This maximum occurred less than 1% of the time, so corrections due to beam steering were neglected.

C. Target

A gas-buffered liquid deuterium target was used. A schematic diagram of the target is shown in fig. 9. The inner walls of the target were of 2 mil mylar, the outer walls of 5 mil mylar. The target flask was situated in a vacuum chamber with a 20 mil mylar exit window. Liquid hydrogen was used to condense deuterium. The liquid deuterium (LD_2) was stored in a reservoir above the target flask and entered the flask via a fill line at its bottom. A line from the top of the target ran through a valve to the top of the reservoir. Normally the valve was open so that deuterium that vaporized was vented. But, for target empty runs, the valve was closed so that the vapor pressure of the boiling deuterium forced the LD_2 out of the flask and back up into the reservoir.

The density of the LD_2 was determined by periodically monitoring the flask pressure. Normally this pressure was 17 inches of Hg below atmospheric pressure. Typical variations were of the order of one inch. This corresponds to a LD_2 density[23] of $0.1677 \pm .0005$ g/cm^3.

Target thickness was dictated by a compromise between competing desires for a high counting rate, on the one hand, and low energy loss and multiple scattering of the doubly charged final state ^{3}He, on the other hand. A 1/2-in. thick target was used.

0 0 1 4 3 0 0 9 5 4

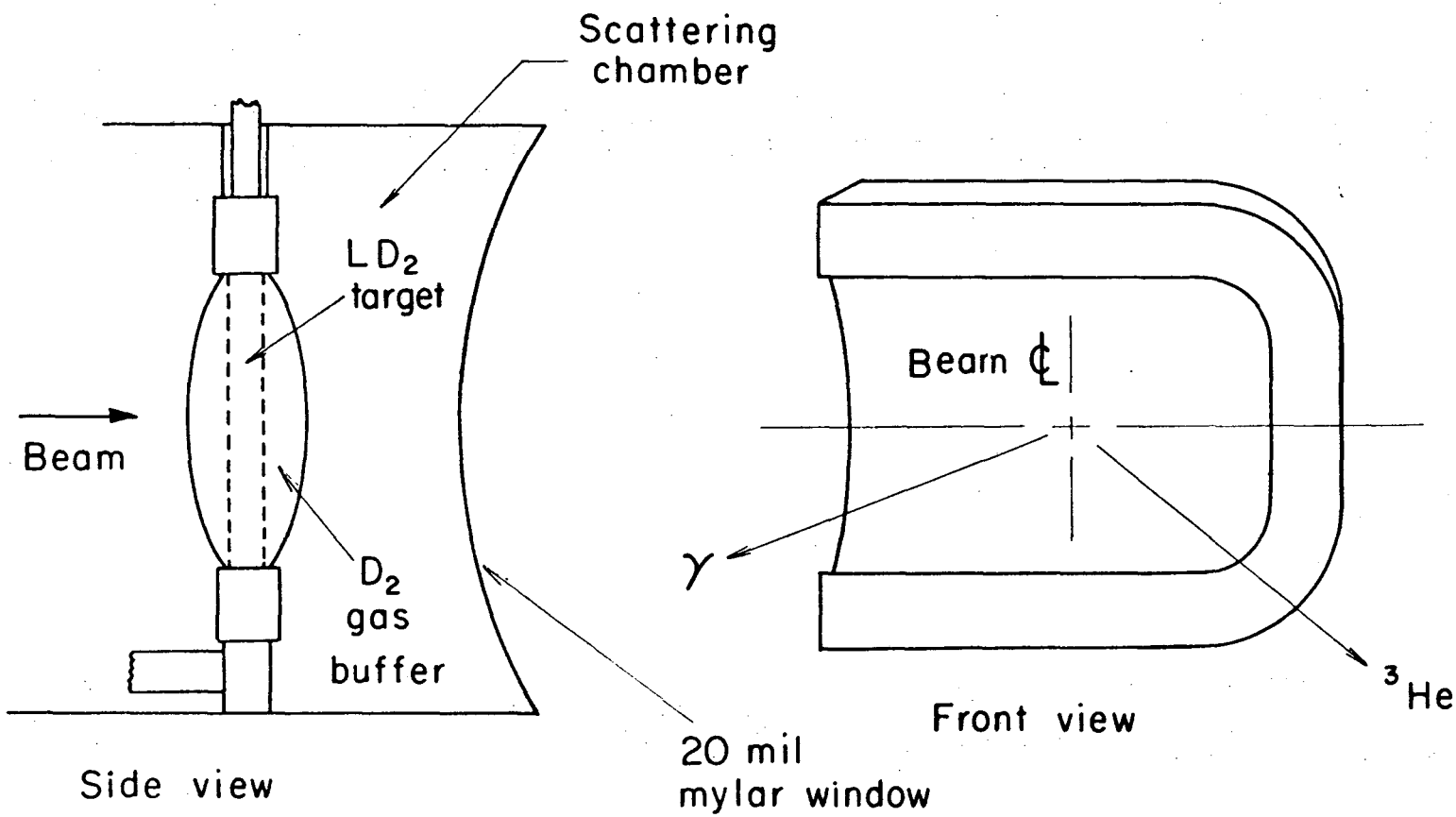

XBL737-3280

Fig.9 Schematic diagram of the deuterium target.

Target thickness (actually the product of target thickness and beam intensity) was continuously monitored during the experiment by measuring the proton-deuteron elastic scattering rate. A schematic diagram of the apparatus is shown in fig. 10. The deuteron telescope consisted of four (12 in. × 12 in., 1/8-in. thick) Pilot-B scintillators in coincidence. Two additional counters (14 in. × 14 in., 1/8-in. thick) were used in anti-coincidence. The proton telescope consisted of three (6 in. × 6 in., 1/8-in. thick) scintillators in a coincidence requiring a signal in at least two of them. Two counters (7 in. × 7 in., 1/8-in. thick) were in anti-coincidence. The degrader, R and ΔR, was selected so that a "slice" of range about the Bragg peak was accepted at the position of the last coincidence counters. The degrader ΔR stopped the particles. Copper and Lucite degraders were used for the deuteron and proton telescopes respectively. The proton telescope defined the solid angle for the reaction. A Monte Carlo program, which included the energy spread, size, and divergence of the beam, was used to check the mapping of the proton telescope onto the deuteron telescope. In addition, the effects of beam mis-steering and variation in the degrader R were checked experimentally and were found to be negligible.

A schematic diagram of the electronics associated with these counters is shown in fig. 11. Accidental coincidences were counted and corrected for. The correction was always less than 10%. The ratio of the target full to target empty proton-deuteron rate was 14:1. The proton-deuteron rate per unit of incident proton beam, as measured by the ion chambers, was constant throughout the course of the experiment to within 0.5%.

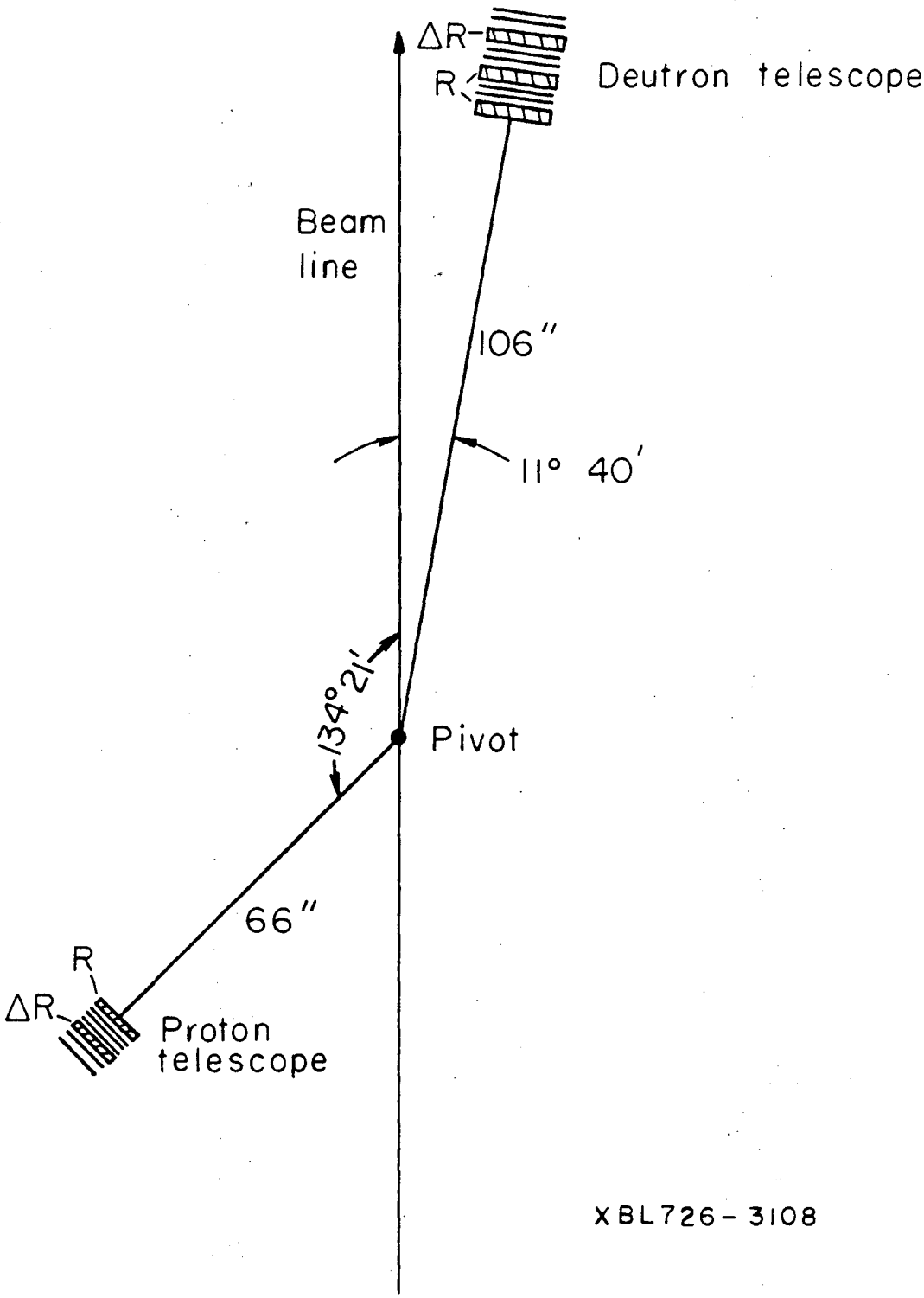

Fig.10 Schematic diagram of the apparatus for monitoring the target thickness.

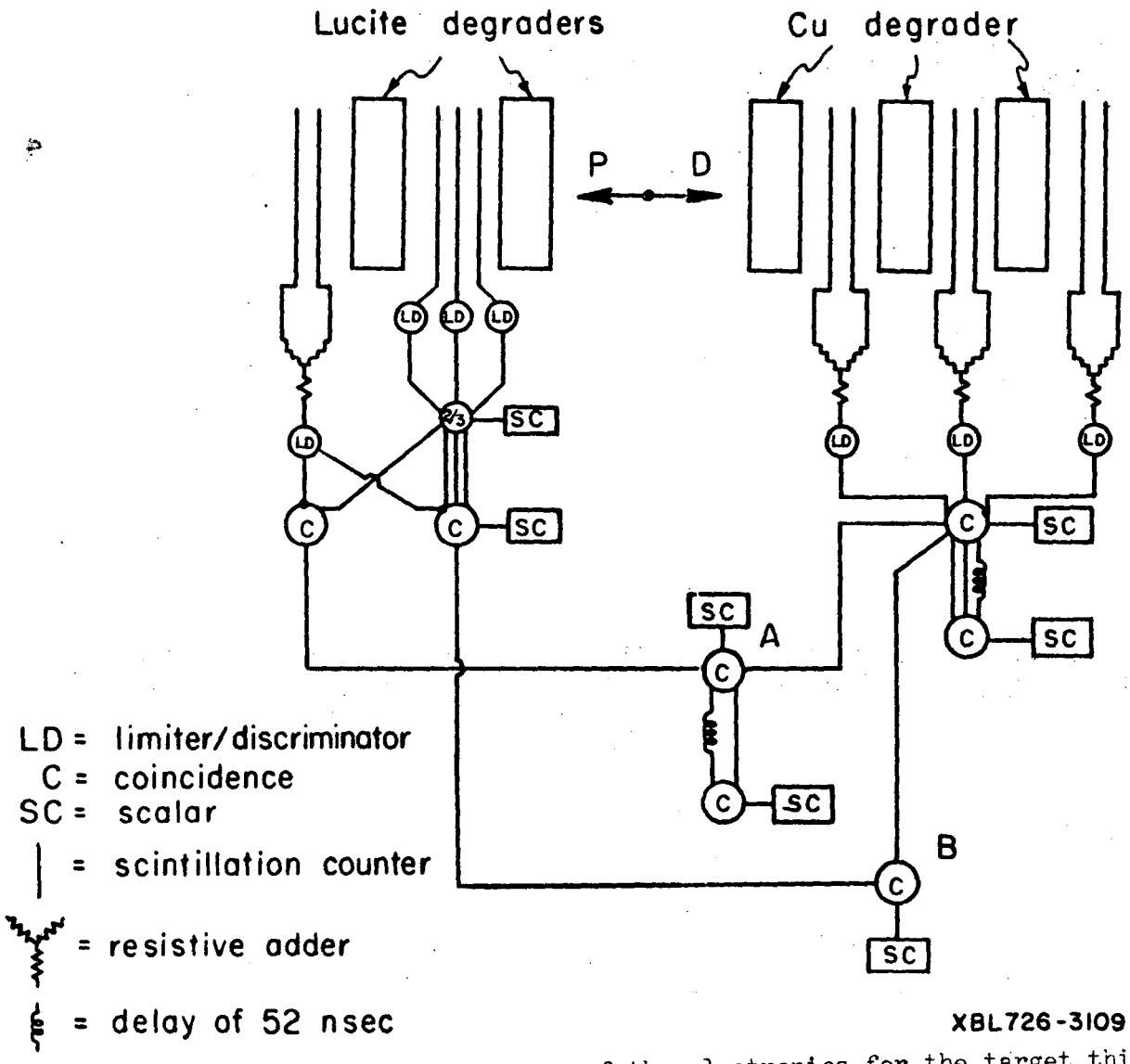

Fig.11 Schematic diagram of the electronics for the target thickness measurement.

D. Helium Spectrometer

1. Magnetostrictive Wire Spark Chambers

The ^{3}He trajectory was determined by two identical magnetostrictive wire spark chambers as shown in fig. 5. The chambers were constructed at LBL.[24] Each consisted of two gaps and four wire planes. Each plane was formed by 3 mil aluminum wire at a spacing of 40 mils. The first plane had wires 30° with respect to the vertical and was grounded. The second plane had wires 30° with respect to the vertical, and 60° with respect to the first plane. This plane and the succeeding plane, which had horizontal wires, were pulsed with high voltage. The last plane had vertical wires and was grounded. The active area of each chamber was 26 in. × 40 in. A sheet of aluminized mylar was placed close to each wire plane to improve the uniformity of the electric field in the chambers.

2. Energy-Loss Counter

An energy-loss (DEDX) counter, following the spark chambers, was used to select doubly charged particles. This counter consisted of 26 in. × 26 in. Pilot-B scintillator, 1/8-inch thick. The scintillator was viewed by a single 5-inch phototube via a folded Lucite light pipe.

3. Helium Energy Counter

A thick, large area plastic scintillation counter was used to stop and measure the energy of the ^{3}He particles. An exploded view of the mechanical construction of the counter is shown in fig. 12. The active area of the counter, Pilot-Y scintillator was

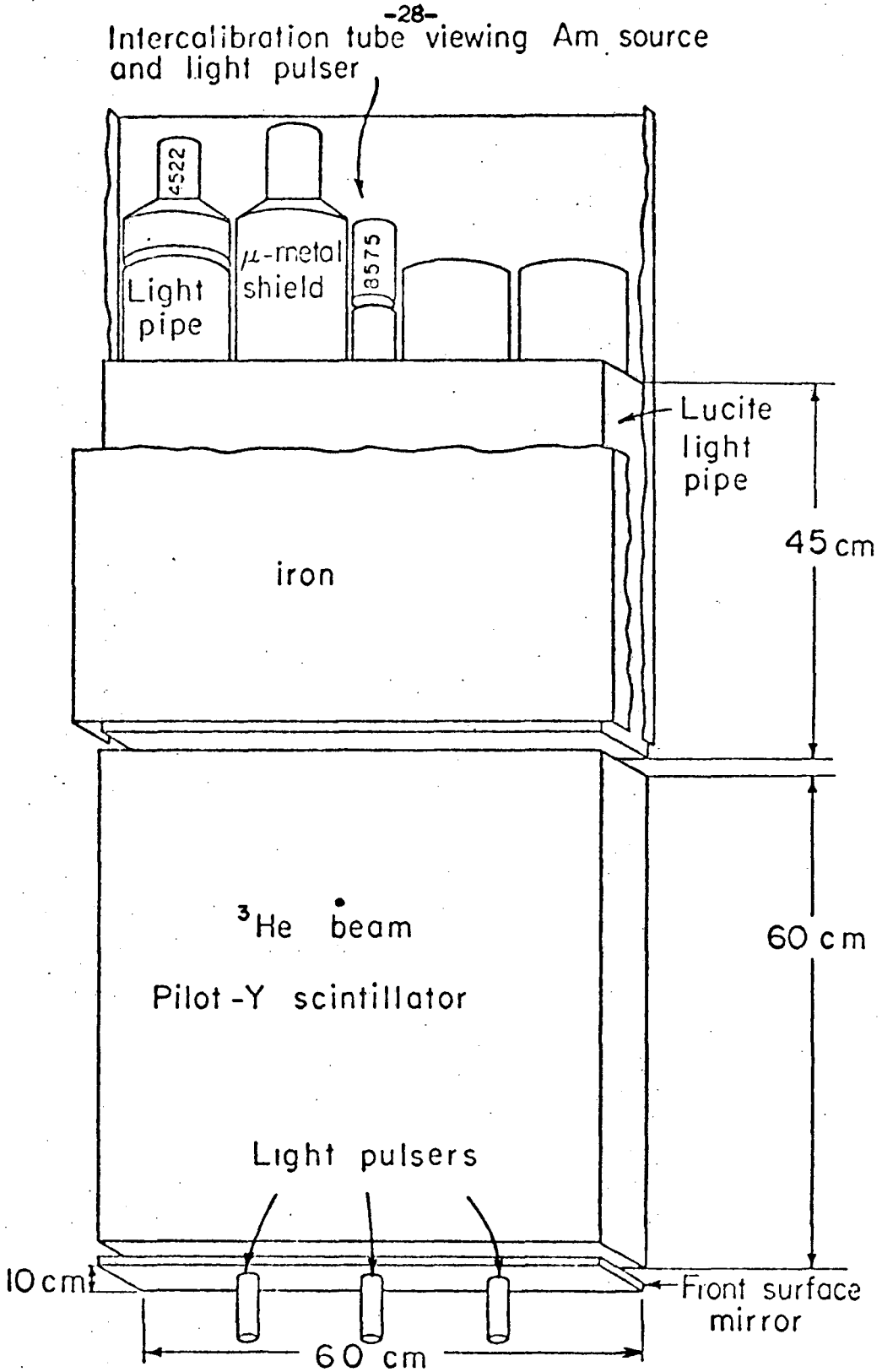

Fig.12 Exploded schematic diagram of the He-counter

24 in. × 24 in. and was 4-3/16 in. thick, which is just thick enough to stop 430 MeV ^{3}He particles. The energy resolution of the counter was 6% FWHM for 130 MeV ^{3}He particles and improved only slightly to 5% FWHM at 250 MeV. Pulse height observed in the counter was a function of position. The counter response was mapped in a 462 MeV proton beam, which deposited 32 MeV of energy in the counter, and the data was used to correct the response[25] of the counter so that the non-uniformity was less than 10%. Nuclear interactions of the ^{3}He particles in the scintillator caused inefficiencies. A typical spectrum for a well-collimated, monochromatic 114.6 MeV ^{3}He beam is shown in fig. 13. The percentage of counts in the tails (all counts below the dashed line in fig. 13 were considered to lie in the tails) was determined for several energies of ^{3}He. The results are shown plotted against scintillator range in fig. 14. The gain of the counter was monitored using a pulsed Argon lamp and an Americium source. The construction and performance of the counter are described in detail elsewhere.[26]

4. Anti-Coincidence Counter

A large (26 in. × 26 in. × 3/8 in.) Pilot-B scintillator was used immediately behind the He-counter to eliminate events which produced charged particles out the back of the He-counter. The counter used three 2-inch phototubes.

E. Photon Detector

Two hodoscope spectrometers were used for photon detection. Their design is shown schematically in fig. 15. They were composed of a sequence of: a veto counter, V, for charged particle

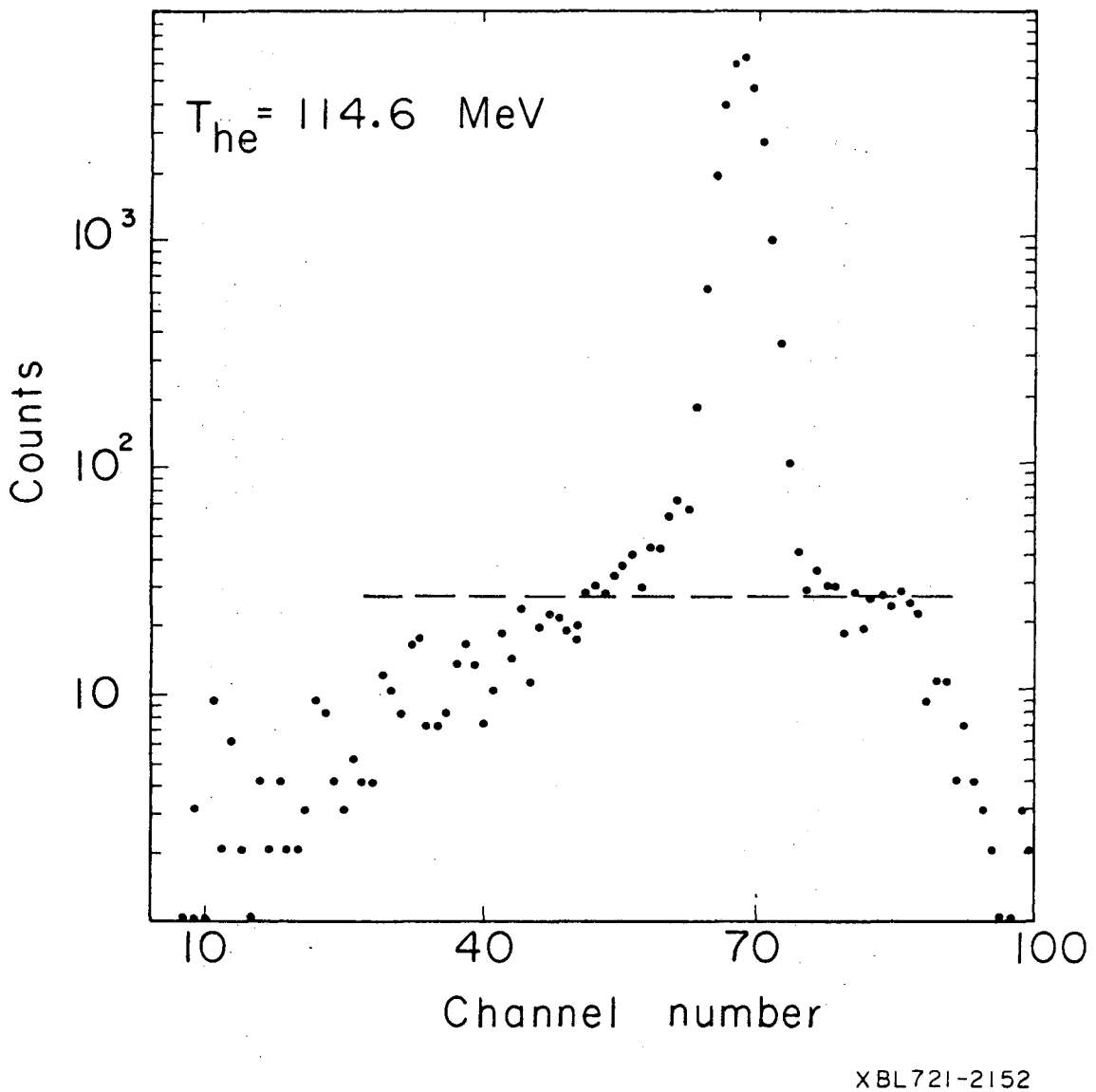

Fig.13 He-counter spectrum for a well-collimated, monochromatic 114.6 MeV ^{3}He beam.

0 0 0 4 3 0 0 9 5 8

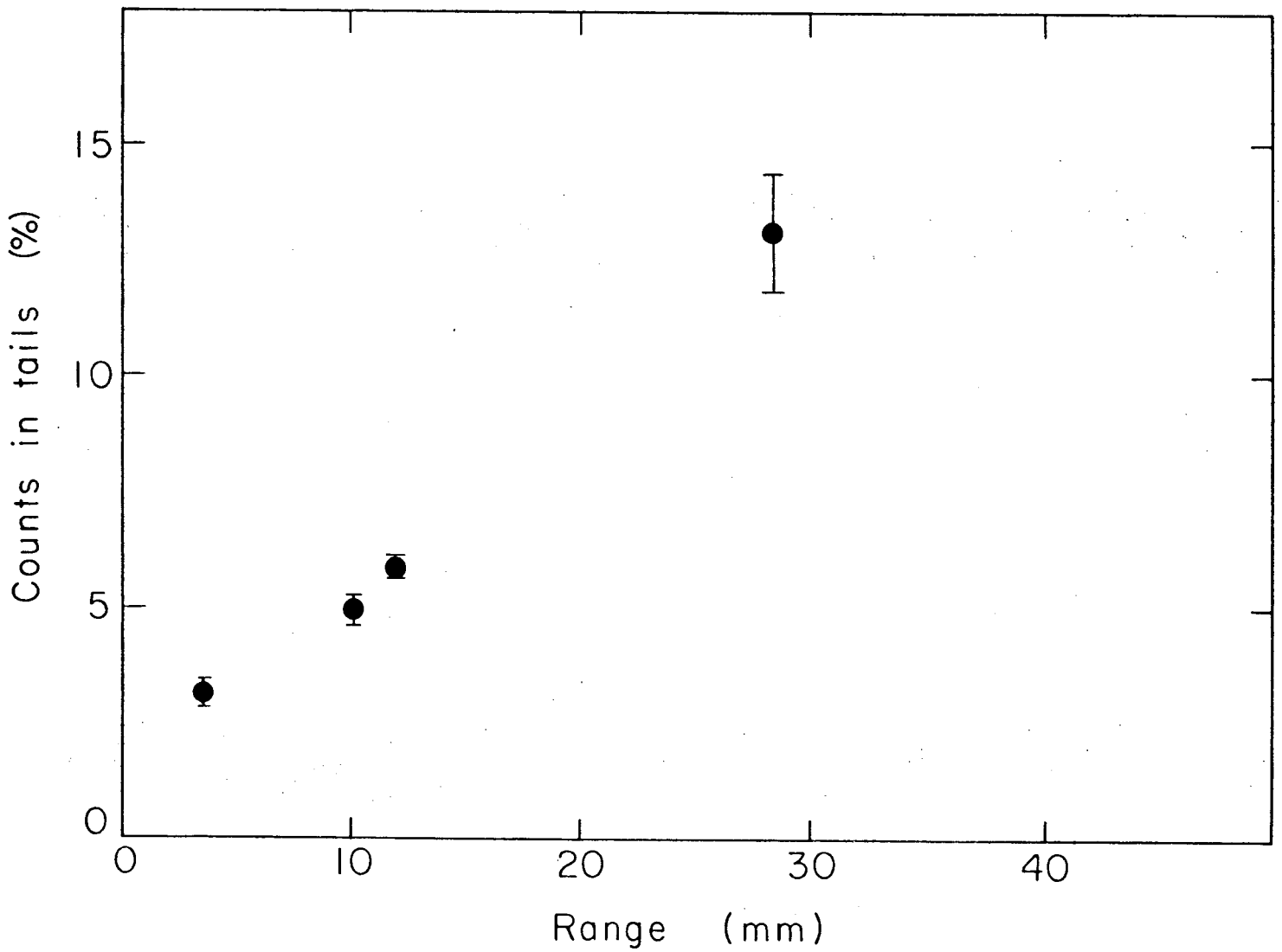

XBL729-4041

Fig. 14 Percent of ^{3}He events in the tails -vs- range in scintillator.

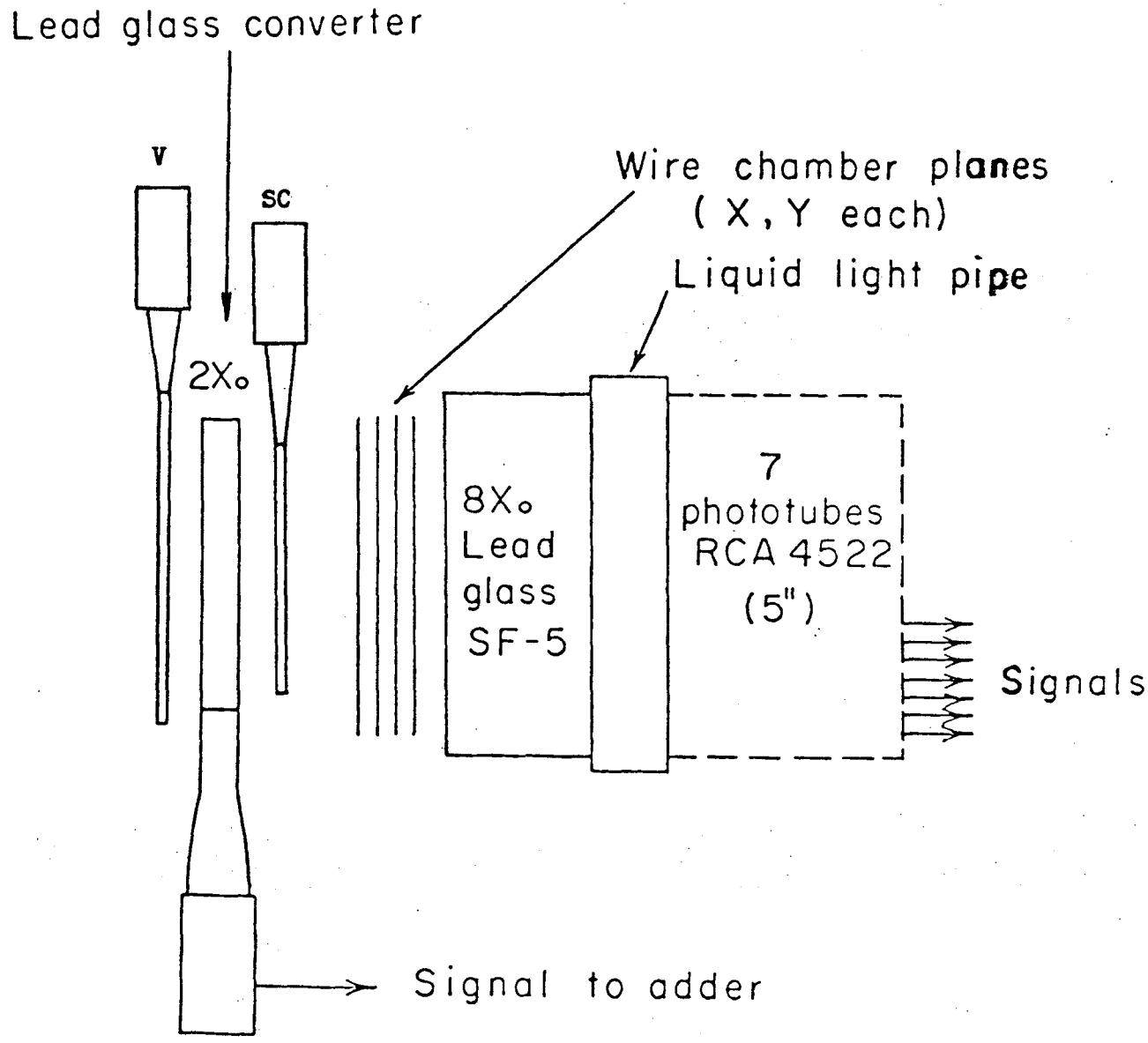

Fig.15 Schematic diagram of the photon counter.

rejection; a 2-inch thick, 2 radiation-length slab of lead glass for both conversion and pulse height information; a scintillation counter, SC, for a photon conversion trigger; a set of magnetostrictive wire spark chambers for photon localization; an 8-inch (8 radiation-length) thick block of lead glass. Each photon spectrometer was mounted on a moveable pivot arm and could be rotated from 23° to 120° with respect to the beam. The conversion efficiency of the 2 radiation-length lead glass converter was determined using a tagged photon beam.[27] Conversion efficiency is shown as a function of photon energy in fig. 16. For the $p + d \rightarrow {}^3He + \pi^0$ analysis the position of the photon conversion was not used. The only relevant fact was whether a photon struck the counter, was converted, and produced charged particles in SC.

F. Running Conditions

The use of two photon counters allowed for simultaneous collection of data in two angular regions. Furthermore, since each photon counter setting included a large range of center-of-mass angles, only three photon counter angles were analyzed to obtain a center of mass angular distribution for an incident proton energy of 462 MeV. In addition, partial angular distributions were obtained for incident proton energies of 377 and 575 MeV.

The requirements for a trigger were: a coincidence between the DEDX counter, He-counter and the photon SC counter, with no simultaneous count in the photon veto counter or in the He veto counter. For each kinematic setting, the pulse from the DEDX counter was required to exceed a given threshold and the He-counter pulse was required to lie

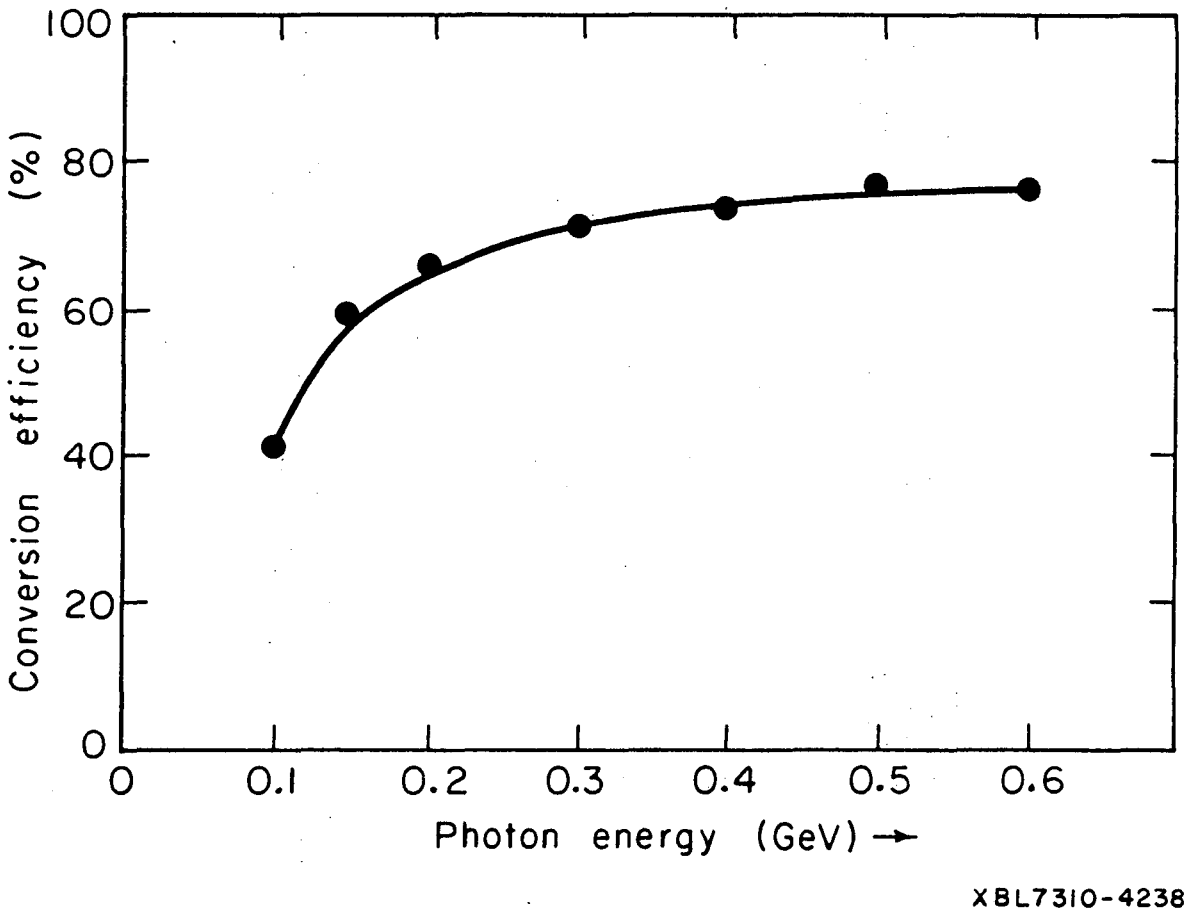

Fig.16 Photon conversion efficiency -vs- photon energy.

within a given range. A schematic diagram of the basic electronics is shown in fig. 17. Bits were set to indicate which photon counter initiated the trigger. For each event, digitized spark information, time of flight difference between the He and photon arms, and pulse heights in the He, DEDX, and photon counters were stored on magnetic tape.

Periodic checks of the helium-photon coincidence timing were made using proton-proton scattering as a reference. Also the proton beam energy was measured several times.

Data were taken with the flask both full and empty.

Periodically throughout the course of the experiment, the two photon counters were interchanged in order to average out any inherent systematic effects. Subsequent analysis showed no discrepancies between results from the two counters.

III. Data Analysis

A. General

The data analysis consisted of taking the experimentally measured quantities and from them extracting the kinematic quantities characterizing the event. These quantities were then compared with the predicted quantities, based on the assumption that the event resulted from the reaction $p+d \rightarrow {}^3He + \pi^o$. If a goodness-of-fit criterion was satisfied, the event was accepted. Fitting was done with a least-square routine with constraints. The measured quantities were: incident proton energy, proton angle in the horizontal plane, ${}^3He$ kinetic energy and scattering angle. No photon characteristics were

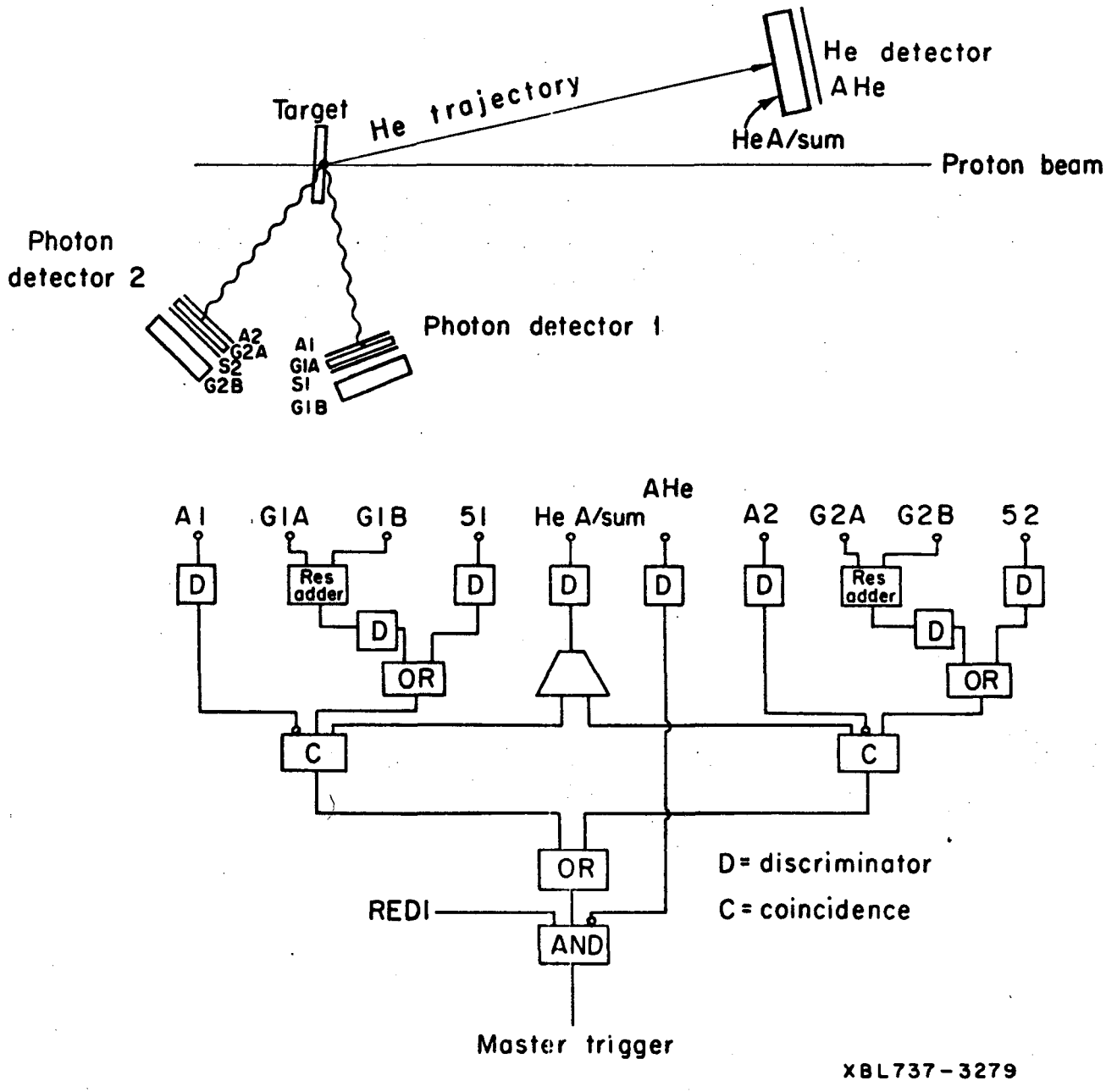

Fig.17 Simplified schematic diagram of the basic electronics.

used, other than the fact that one triggered the photon counter. The experimental data which were recorded on magnetic tape for each event consisted of: 1) bookkeeping entries such as run number, event number, 2) the actual scattering data which included digitized spark information, pulse heights from the photon, DEDX, and He-counters, the presence in the trigger of the first, second or both photon counters, and time-of-flight information. Provisions were made to record six sparks from each of the wire planes of the He spark chambers.

A computer program was used to reconstruct each event from these data. The digitized spark information was used to compute the spark positions in the chambers. A line was determined from sparks in each He chamber. The intersection of this line with the target was the interaction point. The position of this point in the horizontal plane was used to make a minor correction to the direction of the incident proton in the horizontal plane. The assumption was made that the proton lay in the horizontal plane. The angle between the proton direction and the Helium trajectory was the scattering angle. The proton energy was computed by making a correction to the average proton energy for the entire run. This correction was based on the position of the interaction point in the target. The ^{3}He kinetic energy was calculated from the pulse height in the He-counter. This calculation was based on a calibration of the counter using ^{3}He particles of known energy. The ^{3}He kinetic energy was corrected for energy loss in the material along its trajectory from the production point in the target to the counter. For purposes of energy loss calculations for both the ^{3}He and the incident

proton, the interaction point was assumed to lie on the proton trajectory at a point one-half of distance through the target. The event was rejected if the goodness of fit criterion was not satisfied. For each accepted event, the scattering angle of the ^{3}He in the center-of-momentum (CM) system was calculated, and the events were binned according to this angle. The geometric acceptance of the system was calculated as a function of the ^{3}He CM angle by a Monte-Carlo technique. Finally the differential cross section was computed.

B. Helium Trajectory

The ^{3}He trajectory was determined by locating that straight line through the two chambers that best fit the spark locations. The path of the ^{3}He particle was never more than 6° from the perpendicular to the chamber planes. Hence the approximation was made that these wire planes lay at the central plane of the chamber. This reduces the trajectory problem to locating a point in each chamber which best fits the spark positions in that chamber. In locating the path of a particle through a chamber with four wire planes, each having wires running in different directions, one has a redundancy of information. This reduncy was used to resolve ambiguities in multi-spark events and to improve efficiency and accuracy.

For each event there could be zero to six sparks per wire plane. Each spark determined a line or "wire", parallel to the chamber wires, on which the spark was located. A point, P(x,y), was found for which the sum of the squares of the distances to the wires was a minimum. The four chamber planes determined four equations of the form

$$A_i X + B_i Y = C_i , \qquad i = 1,4, \qquad (1)$$

where A_i and B_i are the direction cosines of each of the four wires. In matrix notation Equation 1 is written

$$MP = C$$

where $$M = \begin{bmatrix} A_1 & B_1 \\ A_2 & B_2 \\ A_3 & B_3 \\ A_4 & B_4 \end{bmatrix} , \quad P = \begin{bmatrix} X \\ Y \end{bmatrix} , \quad \text{and } C = \begin{bmatrix} C_1 \\ C_2 \\ C_3 \\ C_4 \end{bmatrix}$$

This system of equations, however, is overdetermined and, in general, has no solution. If Equation 1 is modified,

$$MP - C = r , \qquad \text{where } r = \begin{bmatrix} r_1 \\ r_2 \\ r_3 \\ r_4 \end{bmatrix} ,$$

there exists[28] a unique solution P, which minimizes the sum of the squares of the residuals, r_i. The solution can be written as

$$P = M^I C,$$

where M^I is the generalized inverse of M.

Physically, the residual r_i is the perpendicular distance from the point P to the wire in plane i. If any of the r_i was greater than a

specified fit parameter, the point involved was eliminated from further consideration.

Having found a point, the wires used in determining it were eliminated from further consideration. After all permissable fits had been found involving four wires, fits were sought using three wires. Finally, if no three or four wire fits were found, intersections of two wires were used.

A point from each of the two chambers determined a possible ^{3}He trajectory. Only those that pointed to the target volume were further analyzed.

C. Helium Energy

The helium counter was calibrated in a well-collimated, monochromatic ^{3}He beam at two energies: 69 MeV and 130 MeV. At higher energies, tagged ^{3}He particles from the reaction $\alpha + p \rightarrow {}^3He + d$ were used. These data spanned a ^{3}He energy range of roughly 100 - 265 MeV.

The scintillator response data were fit using the parametric formula[26]

$$\frac{dL}{dx} = g\,(dE/dx)(1 + B\,dE/dx)^{-1}$$

where

$\frac{dL}{dx}$ = Fluorescent light energy emitted per unit path length,

g = overall gain of the counter,

dE/dx = ^{3}He energy loss per unit path length

B = Scintillator saturation parameter.

For each datum the integral,

$$PH = \int_0^V \frac{(g \cdot M \cdot \beta)\, d\beta}{(1-\beta^2)^{3/2}(1+\beta \cdot dE/dx)}$$

where,

M = ^{3}He mass

V = Measured ^{3}He beta at the counter face,

was calculated and compared with the measured pulse height. The betas of those ^{3}He particles generated by the reaction $\alpha + p \rightarrow {}^3He + d$ were calculated on the basis of the measured kinematic quantities (kinetic energy and direction of the α, and scattering angles of ^{3}He and d). A least-squares minimizing routine, which treated g and B as adjustable parameters, was used to minimize the quantity,

$$\chi^2 = \sum_i \left| \frac{PH_i^{pred} - PH_i^{meas}}{\sigma_i} \right|^2$$

where,

PH_i^{meas} = Measured pulse height of the i-th datum,

PH_i^{pred} = corresponding pulse height obtained by means of the above integral,

σ_i = standard deviation in units of pulse height of the measured pulse height in the energy region of the i-th datum.

The values of the adjustable parameters giving the best fit were:

$$g = 1.325$$

$$B = 9.566 \times 10^{-3} \ g/cm^3/MeV.$$

D. Geometric Acceptance

The geometric acceptance of the system was calculated by means of a Monte Carlo program. This program included the effects of the proton beam energy spread, spatial distribution of the proton beam at the LD_2 target, and both correlated and random beam divergence. Also included were energy loss and multiple scattering of the scattered ^3He particles. Monte Carlo programs were written by two independent programmers. The results of the programs were consistent to within statistical error (1%).

For each angle at which data was collected, the configuration of the experimental apparatus was specified in the Monte Carlo program exactly as it had been measured for the case of real data. The effective solid angle at each configuration of the apparatus was defined jointly by the Helium counter and the photon counters. For a given event an interaction point (x,y,z) in the target and a direction ($\cos\theta$ and φ) were chosen for the ^3He particle. If the ^3He struck the Helium counter, the program proceeded with the uniform decay of the π^0 in its CM system. The path of each photon was traced to determine whether it was intercepted by either of the two photon counters. The conversion efficiency of the photon counter was folded into the geometric acceptance of the apparatus at each setting.

A typical geometric acceptance curve with the photon conversion efficiency folded in is shown in fig. 18. When actually extracting the

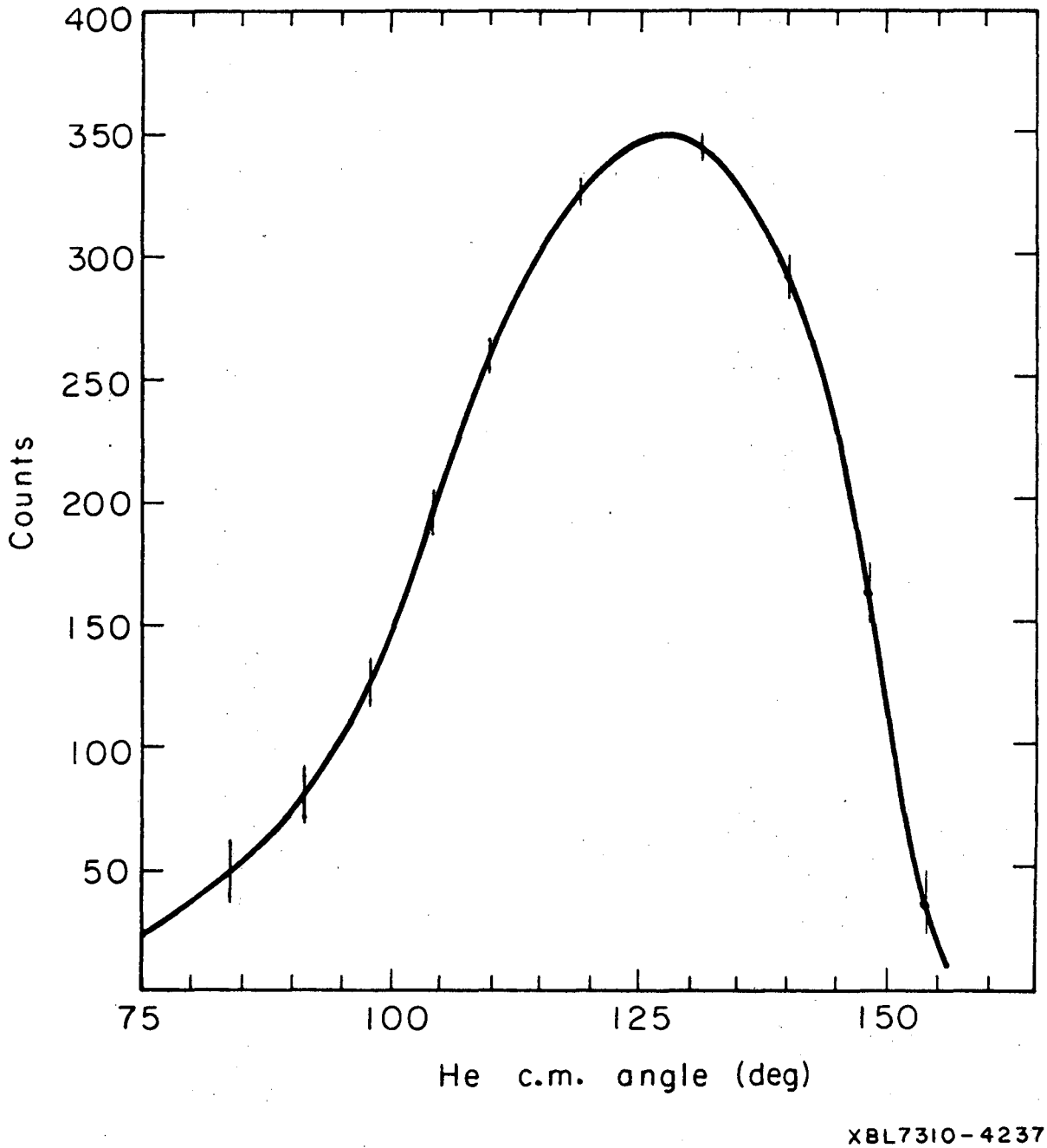

Fig.18 Typical geometric acceptance.

cross section, only the region of the solid angle near the peak was used, where the statistical error is less than 10%.

E. Least-Squares Kinematic Fitting.

The set of processed data from the helium chambers, energy-loss counter, and He-counter was subjected to two criteria before further analysis. First, the ^{3}He trajectory, as computed from the spark chamber information, was required to originate in the target. This requirement, rather than the more stringent one that the trajectory originate in the area defined by the spatial distribution of the beam at the target, was used to insure that no potential events were lost as a result of trajectory reconstruction errors caused by multiple scattering and finite spatial resolution in the chambers. Second, the pulse in the energy-loss counter was required to be above a given threshold value for each kinematic setting. A typical energy-loss spectrum with the threshold indicated is shown in fig. 19. The superimposed points indicate the same spectrum resulting from a relatively clean sample of ^{3}He (obtained by means of a χ^2-cut described below).

The events satisfying these requirements were referred to a common coordinate system, which had as its origin the "pivot" (the point about which the photon counter rotated and to which the survey referred). The coordinate system and relevant angles are shown in fig. 20.

The measured quantities were:

θ_1

θ_2, φ_3

T_1

T_3

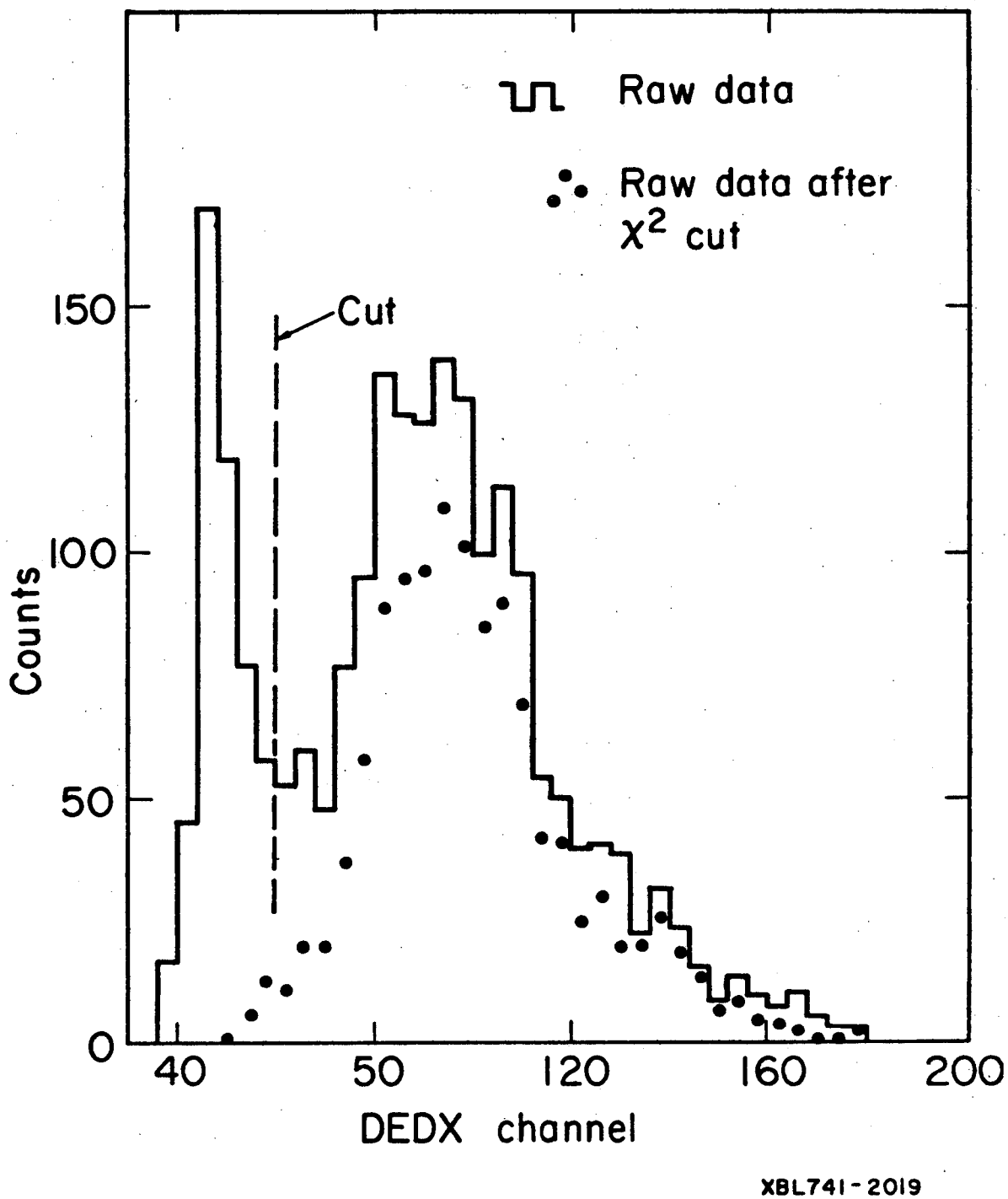

Fig.19 Typical DEDX cut.

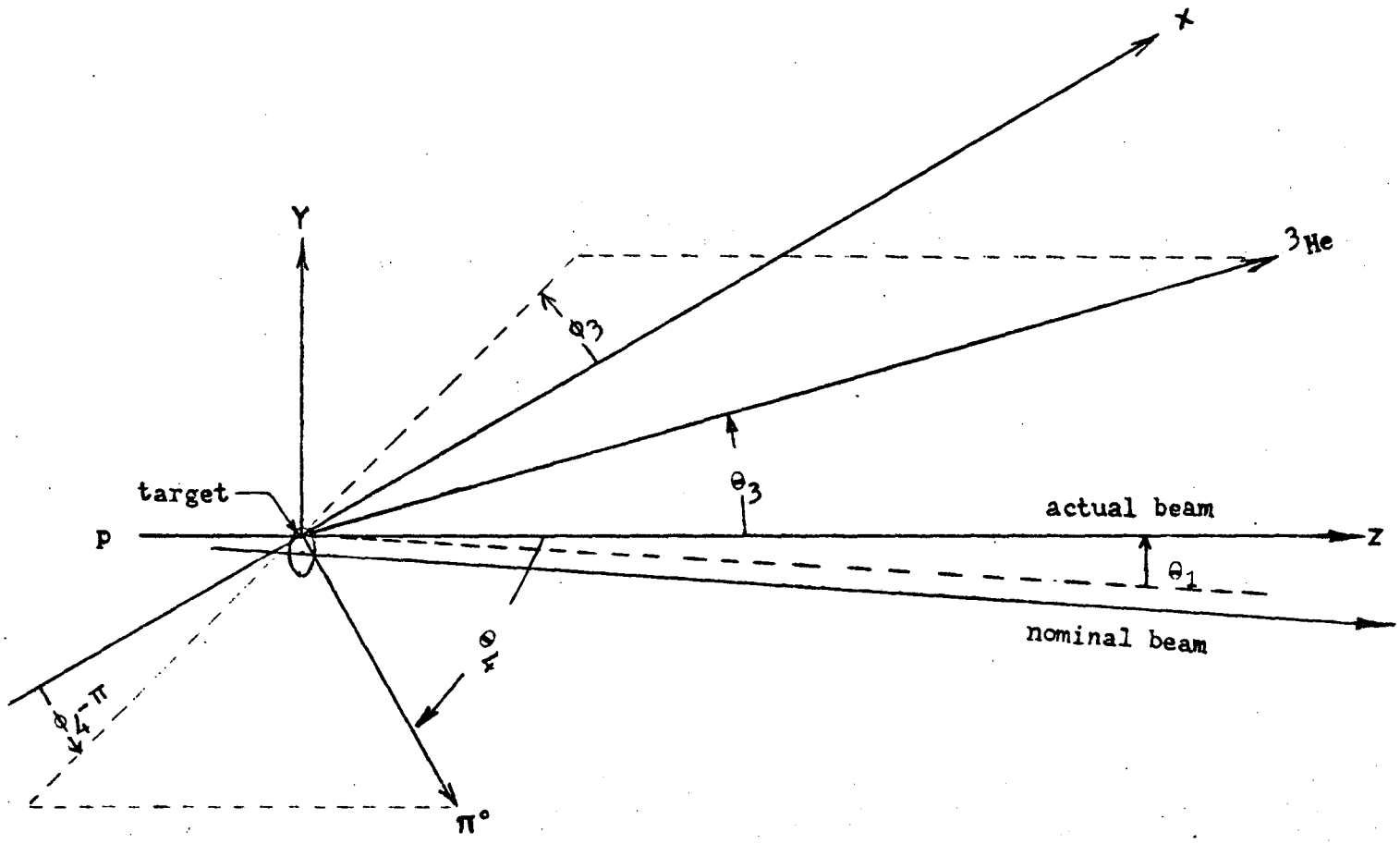

Fig.20 Coordinate system used in the kinematic fitting program.

where the subscripts 1 and 3 refer to the incident proton and scattered ^{3}He respectively. The incident proton was assumed to lie in the horizontal plane, and a correction was made for the divergence angle 0_1.

For a p+d $\rightarrow$ ^{3}He + π^0 event, the measured quantities as expressed above are subject to energy-momentum conservation. The equations are:

Energy: $$E_1 + M_2 = E_3 + E_4 \quad (1)$$

Momentum:

X-component: $$P_3 \sin\theta_3 \cos\phi_3 + P_4 \sin\theta_4 \cos\phi_4 = 0 \quad (2)$$

Y-component: $$P_3 \sin\theta_3 \sin\varphi_3 + P_4 \sin\theta_4 \sin\varphi_4 = 0 \quad (3)$$

Z-component: $$P_1 - P_3 \cos\theta_3 - P_4 \cos\theta_4 = 0 \quad (4)$$

where the subscripts 2 and 4 refer to the target deuteron and the π^0 respectively. E_i is the total energy of the i-th particle. The only independent variables in equations 1-4 that were not measured are P_4, θ_4, and φ_3. Thus the four equations are overdetermined and a fitting procedure must be utilized to obtain the optimal solution.

The method used was that of least-squares fitting subject to the non-linear constraints of energy-momentum conservation. This is a standard procedure in bubble chamber physics.[29] Three of the equations of energy-momentum conservation are required to determine the unmeasured kinematic variables. The remaining one is used as the equation of constraint in the fit, giving what is called a "one-constraint fit". Equation 1 above was used as the constraint equation. In addition to fitting the data for each event to the hypothesis that it resulted from

the reaction $p+d \rightarrow {}^3He + \pi^0$, a "goodness-of-fit" number (χ^2-value) was calculated for each event. A histogram of this χ^2-value for a typical run is shown in fig. 21. The Monte Carlo data were normalized to the real data by requiring the same number of events with χ^2 less than 10. A description of the fitting procedure is given in more detail in Appendix C.

F. Efficiencies

1. General

In calculating the cross section, the detection efficiency of the apparatus must be used. This efficiency can be considered as the probability of detecting the desired event, given that it has occurred. One important factor in this detection efficiency is the geometric acceptance of the apparatus. This has been discussed in section D above. The remaining efficiencies include the detection efficiencies of the apparatus. The photon conversion efficiency has been treated in section II.E. The efficiency of the SC counter, described in the same section, was essentially 100%. The helium spark chamber efficiency will be discussed in section 2 below. The efficiency of the energy-loss counter for ${}^3He$ particles of energy in the range of interest of the experiment was 100%. A correction, however, was made (section I below) for ${}^3He$ break-up in the material before the counter, since the resulting singly charged particles would not trigger the counter. Similarly, ${}^3He$ particles undergoing nuclear interactions in the He-counter could fail to be detected at the correct energy. This is also discussed in section I. For those ${}^3He$ particles not interacting

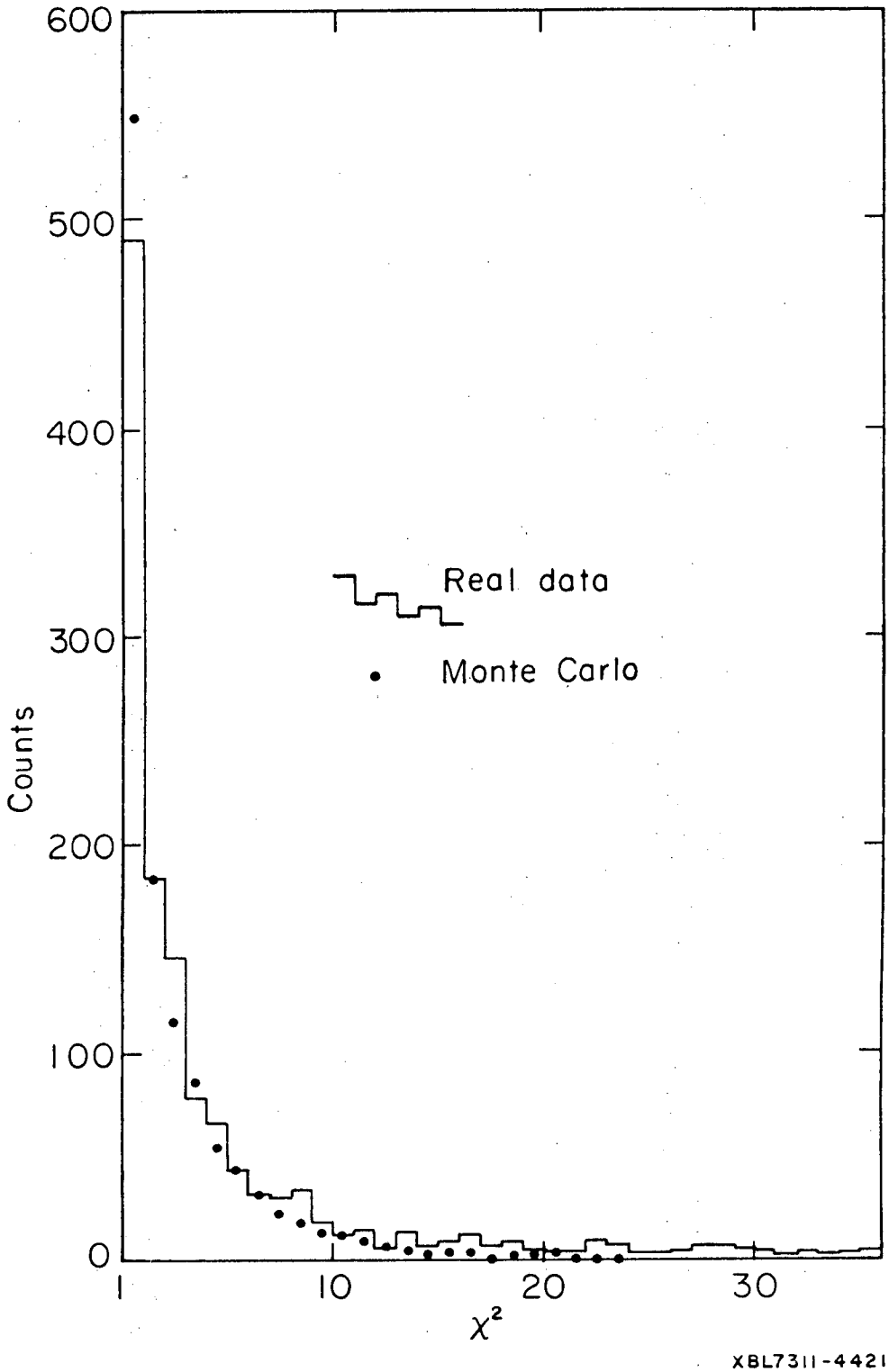

Fig.21 Typical χ^2 spectrum.

strongly in the scintillator, the detection efficiency was considered to be 100%. Finally, the efficiency of the helium veto counter was taken as 100%. The only remaining efficiency was "counting" efficiency. This relates to the efficiency of use of the protons in each beam spill and will be discussed in section 3 below.

2. Spark Chamber Efficiency

The procedure for calculating spark chamber efficiency involved first obtaining a subset of events called probe events, which were used to investigate the efficiencies of individual gaps. A probe event is defined as an event for which at least three of the four gaps (two gaps per chamber) have sparks, and a track reconstructed from the sparks extrapolates to the area defined by the intersection of the beam with the target. This latter constraint is to insure that the probe events result in fact from particles, and not spurious sparks. Given a probe event, either (a) there are sparks in all four gaps, in which case the probe is a positive probe of any gap, or (b) one gap has no spark, in which case the probe is a negative probe of that gap and a positive probe of the three other gaps. The inefficiency of an individual gap is then the ratio of the number of negative test probes for that gap to the number of test probes. The gap efficiencies were then used to compute chamber efficiencies. The chambers were typically 99 - 100% efficient.

3. Counting Efficiency

This efficiency refers to the efficiency with which the protons in each beam spill were used. This is determined by two

factors: the amount of dead time per spill, during which the fast electronics were gated off to allow for spark chamber recharge, pulse height analysis, and data storage; the acceptance of only the stretched portion of the beam spill for data taking.

The system dead time was determined by scaling all potential event triggers as well as those actual triggers that occurred when the system-ready gate was set. For some runs, the dead time was as large as 20%.

The stretched-beam spill of the cyclotron consists of a spike of particles 64 times per second, followed by an approximately uniform flux for about 10 msec. The spike was gated off since the flux in this part of the beam spill was too high for our electronics to register properly. The percentage of protons lost in this way was continuously monitored by the proton-deuteron monitors. When the beam was properly tuned, this loss was never more than 5% and typically only 2%.

G. Background

The event trigger required on the helium side a charged particle which deposited a considerable amount of energy in the energy-loss counter and stopped in the helium-counter. On the photon side the requirement was for a charged particle in the SC counter which did not pass through the veto counter. This is a fairly unique signature at the proton energies at which we operated. The only conceivable background reactions that could leave such a signature, except the reaction (2), are

$$p + d \rightarrow {}^{3}He + n\pi^{o},$$

where n = 1, 2, 3.

The threshold for n - π^o production is given by

$$T_P = \left[(M_{^3He} + nM_{\pi^o})^2 - (M_P + M_d)^2 \right] / 2M_d ,$$

where T_P is the incident proton kinetic energy, n the number of pions. The threshold for single pion production is 198.7 MeV, that for two pion production 415.4 MeV, and that for three pion production 641 MeV. Thus, three pion production is beyond the kinematic range of interest of this experiment. In the case of two pion production, the 377 MeV data is uncontaminated, being below the two pion threshold. At T_P = 462 MeV and 576 MeV the effects of two pion production are negligible compared to those of single pion production. The main reason for this is that the ^{3}He particle associated with two pion production is confined to a much narrower cone in the lab system than in the case of single pion production. As a result, only certain ^{3}He particles from this background reaction undergoing wide-angle multiple scattering could possibly hit the He-counter. Furthermore, the two pion production cross section increases slowly as the threshold energy is exceeded. In addition, significant differences in the kinematics of single and double pion production facilitate the separation of these two reactions on the basis of their respective χ^2-values. For these reasons, two pion contamination was considered to be negligible.

The reaction (2),

$$p + d \rightarrow {}^3He + \gamma ,$$

is a more serious source of contamination. Its cross-section is approximately 5% of that of reaction (1),

$$p + d \rightarrow {}^3He + \pi^o ,$$

and the kinematics of the two reactions are quite similar. For these reasons, no attempt was made to separate events due to the two reactions until the final stage of the anlysis, at which point a correction to the results was made, based on the known cross-section[1] for the reaction (2). The uncertainty in this correction was estimated to be 10%.

H. Cross Section Calculation

The differential cross section for a given setting is determined by the relation

$$N(\theta) = d\sigma(\theta)/d\Omega \times N_B \times Eff \times N_d$$

where:

θ	=	center of mass helium angle
$N(\theta)$	=	number of events
$d\sigma(\theta)/d\Omega$	=	differential cross section at a helium center of mass angle θ
N_B	=	number of beam particles
Eff	=	solid angle × counting efficiency × spark chamber efficiency × ${}^3He$ breakup × photon conversion efficiency
N_d	=	number of target particles = $N_o \times t \times \rho/2$
		N_o = Avogadro's number
		t = target thickness
		ρ = density of liquid deuterium

The ^{3}He center of mass angle for the reaction $p+d \rightarrow {}^3He + \pi^o$ can be calculated from the measured quantities by two different methods: 1) use of the helium energy and scattering angle, 2) use of the beam energy and helium energy. In the first case the center of mass angle is given by the relation:

$$\cos\theta'_{He} = \left[AC \pm \left[A^2C^2 - (A^2+B^2)(C^2-B^2) \right]^{\frac{1}{2}} \right] / (A^2+B^2) ,$$

where

$$A = P'_{He}(1 + \beta^2\gamma^2)$$

$$B = \gamma P'_{He} / \mathrm{Tan}\theta_{He}$$

$$C = -\beta\gamma^2 E'_{He}$$

The primed quantities refer to center of mass quantities. The choice of sign is determined by requiring that the lab helium energy calculated from the derived center of mass angle lie closer to the measured helium energy. In the second case, the expression is:

$$\cos\theta'_{He} = (E_{He}/\gamma - E'_{He})\beta P'_{He} .$$

The method used was that which yielded the smaller error for θ'_{He}. The error in θ'_{He} as a function of θ'_{He} for the methods 1) and 2) is shown in figures 22(a) and 22(b) respectively, for a beam energy of 462 MeV. The errors represent the error in the calculated CM angle resulting from an error of one standard deviation in the measured quantities θ'_{He} and E_{He}.

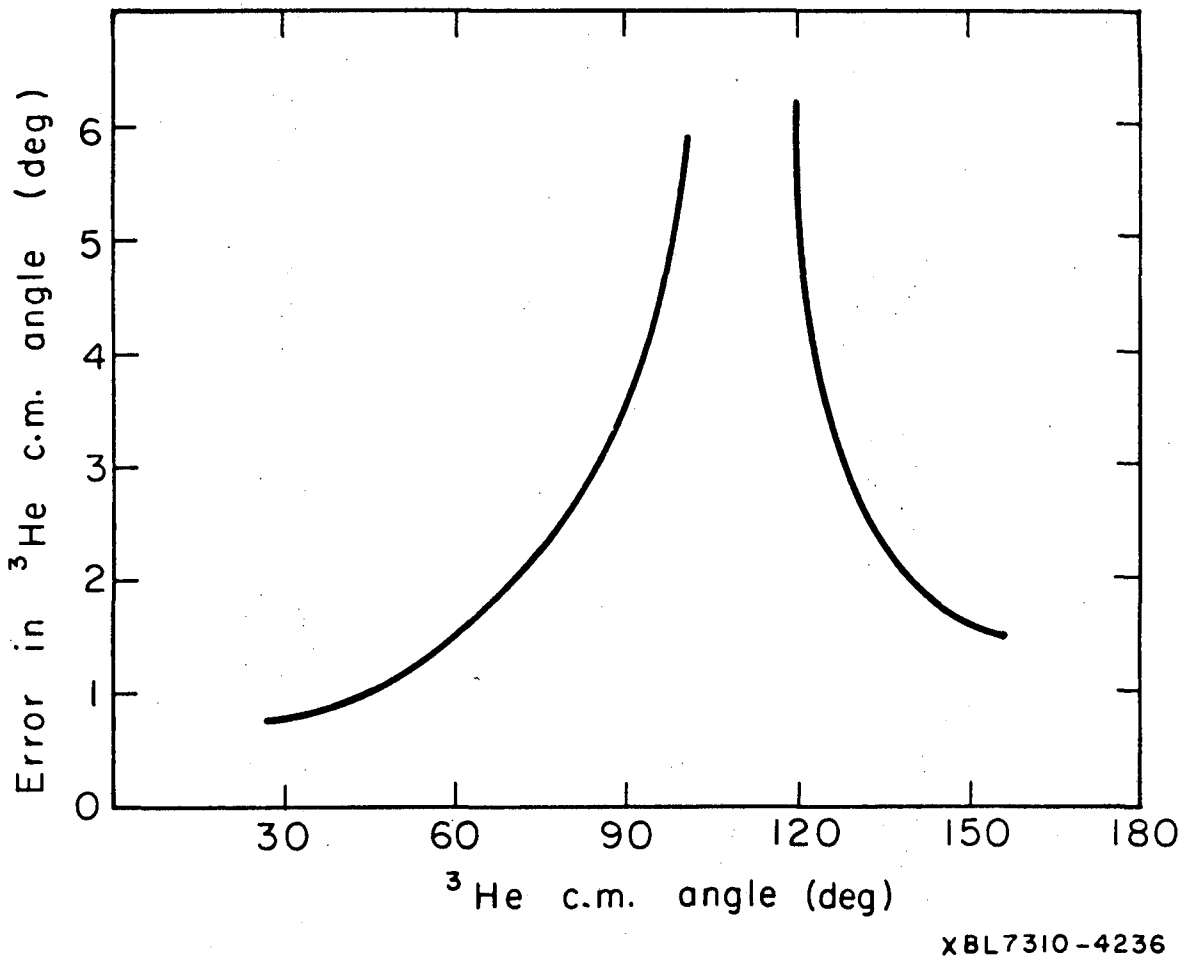

Fig.22(a) Error in the ^{3}He c.m. angle -vs- ^{3}He c.m. angle.

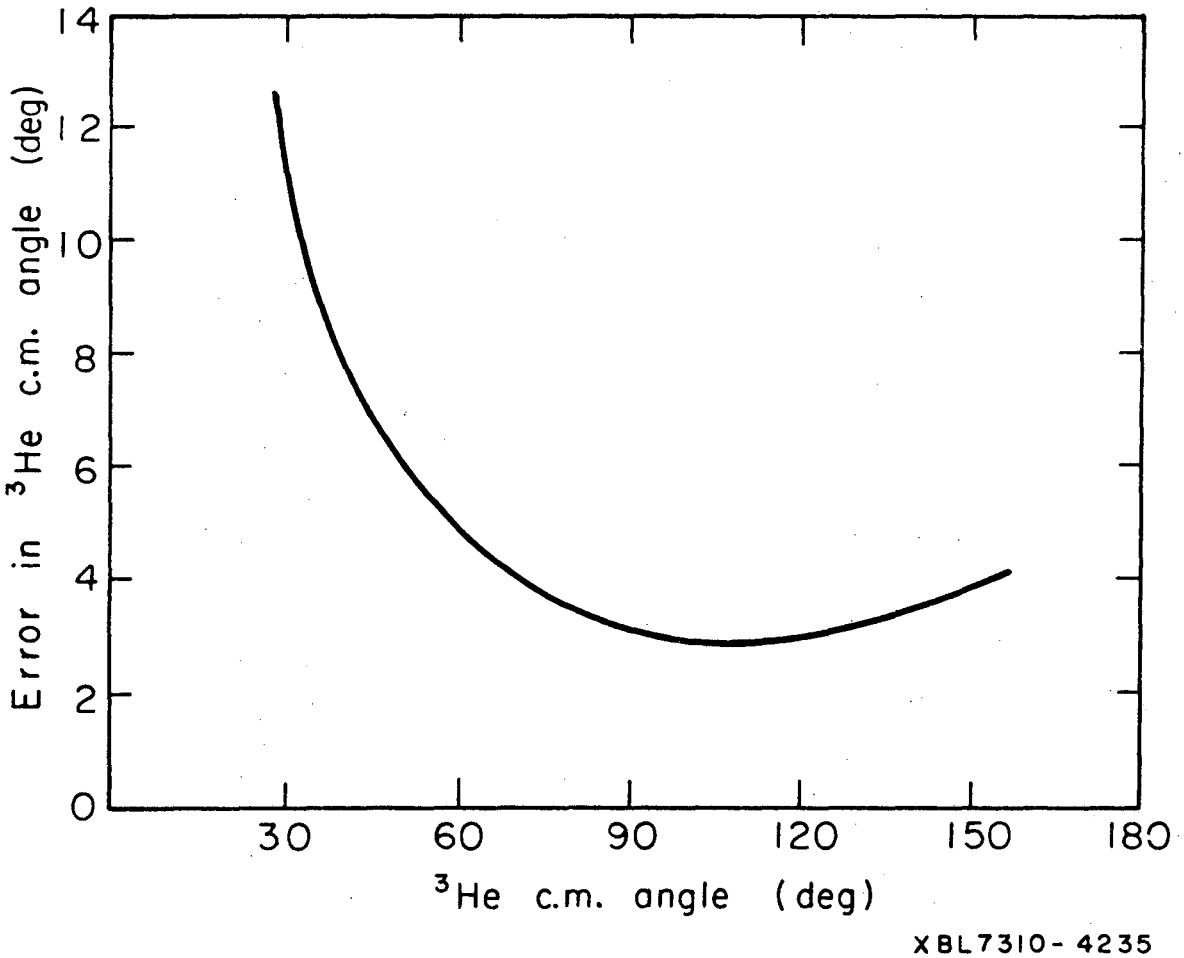

Fig.22(b) Error in the ^{3}He c.m. angle -vs- ^{3}He c.m. angle.

At certain kinematic settings it was possible to detect each of the photons resulting from the decay of the π^0. This required a wide spacing between the two photon counters (about 50°). The minimum opening angle between the two photons, ϕ, occurs in the case of symmetric decay in the lab system. This angle is determined by the relation[30]

$$\cos \frac{\phi}{2} = \beta ,$$

where β denotes the beta of the π^0. For the 462 MeV runs, β was typically 0.9. A separate Monte Carlo program was written to determine the geometric acceptance for two photon detection, and the cross section was calculated based on the double photon trigger for the most favorable kinematic setting at 462 MeV incident proton energy. The results are shown in Table 2 of section IV.

I. Errors and Corrections

1. ^{3}He Break-up

Those ^{3}He particles which underwent catastrophic nuclear collisions and broke-up in the material before the energy-loss counter failed to trigger the system. In the energy range of ^{3}He particles dealt with in this experiment (lowest ^{3}He kinetic energy = 100 MeV, range in CH = 8 mm), the probability that a ^{3}He particle will break up in a given material is roughly proportional to its range in the material. This probability was measured to be 0.0035 ± .001 per mm of CH in the ^{3}He kinetic energy range of 100 - 260 MeV.[26] From the target midplane to the midplane of the energy-loss counter there was a material equivalent of 6.3 mm of CH. The corresponding loss is 2.2 ± 0.6%.

Singly charged particles resulting from ^{3}He break-up did not have sufficient energy to penetrate the He-counter and trigger the veto counter.

2. Efficiency of the Goodness-of-Fit Cut.

Selection of events as genuine p+d $\rightarrow$ ^{3}He + π^o events was based on a goodness-of-fit parameter, χ^2, which was calculated for each event satisfying the target and energy-loss criteria described in section III.E. A typical χ^2 distribution is shown in fig. 21. Superimposed on the χ^2 distribution is a similar distribution generated by Monte Carlo data, which includes an estimate of p+d $\rightarrow$ ^{3}He + γ contamination. The Monte Carlo data was normalized by requiring an equal number of events with χ^2 less than 10 for the two distributions. Those events with χ^2 less than 10 were selected as real events. Monte Carlo data indicate that typically 6% of p+d $\rightarrow$ ^{3}He + π^o events have a χ^2-value greater than 10. These events are primarily due to ^{3}He break-up in the He-counter, resulting in an abnormal pulse height.

As is evident from fig. 21, the real data has proportionately more events with χ^2 greater than 10 than the Monte Carlo data. Typically 25% of the real events have a χ^2 in this region. The majority of these events are attributed to accidental triggers. These spurious triggers were separated into two classes: i) accidental events caused by the detection of a bona fida ^{3}He particle from reactions (1) or (2) in coincidence with an accidental count in the photon arm; ii) all other accidental events. Events of type (i) cannot be distinguished from real events since no kinematic information was obtained from the photon

arm. In general, this type of accidental event will produce a low χ^2-value and will be accepted as a genuine event. Events of type (ii), however, would not be expected to produce a χ^2-distribution peaked at low values.

The degree of contamination of the data from type (i) accidental events was estimated by calculating the accidental trigger rate using the measured counting rate in the photon arm and a Monte Carlo calculated counting rate in the He arm. This rate was based on the measured cross-section. Typically the resultant accidental trigger rate of this type amounted to less than 2% of the measured rate, except for the 576 MeV data, in which case the rate was 18%. This is a consequence of the high beam intensity at this energy. The measured cross-sections were reduced by the fractions corresponding to the accidental trigger rates, and an uncertainty of 20% was assigned to this correction.

Accidental events of type (ii) would not be expected to produce a peaked energy-loss (DEDX) distribution. The DEDX distribution for events satisfying the relation $10 < \chi^2 < 30$ is indeed quite flat, as shown in fig. 23 for a typical run. This behavior was extrapolated to the domain of $\chi^2 < 10$, and an estimate was made of the contamination in this region. This typically resulted in a 5% reduction in the cross-section, with an estimated uncertainty of 20%.

3. Target Thickness.

The thickness of the liquid deuterium target was never measured under run conditions. Although the product of target thickness and beam intensity was quite stable during the run

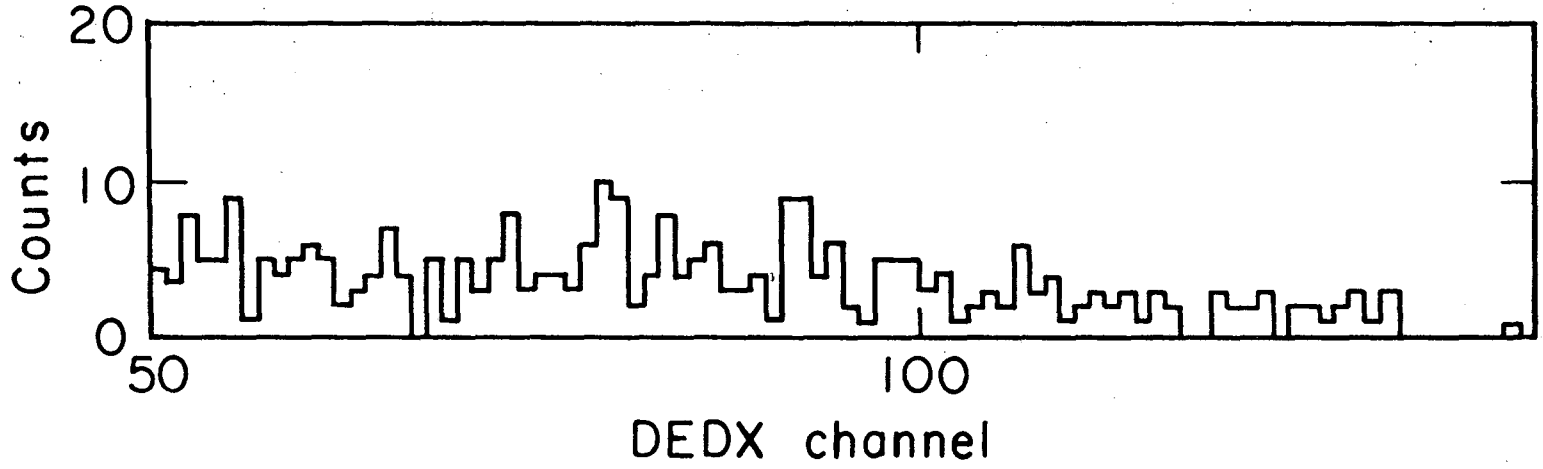

XBL741-2018

Fig.23 Typical DEDX spectrum for events with $10 < X^2 < 30$.

(see section II.C), there is some evidence that the target may have been bulging. An upper limit on the extent of this bulging is 6%. As a result, the cross-sections quoted in section IV may be as much as 6% too high.

4. Target Empty.

Events produced with the target empty were never more than 1% of those produced with the target filled with liquid deuterium. Therefore, events originating from the target walls were neglected.

The corrections to the data, together with the corresponding errors, are summarized in Table 3 of section IV.

IV. Experimental Results

The measured cross sections are given in Table 2. The widths of the angular bins are typically 10°. The errors in the c.m. angle of the ^{3}He are due to multiple scattering. The indicated errors in the cross-sections include a statistical component, from counting statistics and statistical error in the determination of the solid angle, and a systematic component. The systematic errors for each angular bin are given in Table 3. The subgroups within the 377 and 462 MeV data indicate data obtained at different kinematic settings. The last subgroup within the 462 MeV data represents the data resulting from 2-photon analysis.

The data from different kinematic settings show good consistency. There is also good consistency between the one-photon and two-photon results. The experimental results at 377, 462, and 576 MeV are shown in fig. 24.

TABLE 2

Differential Cross-Sections

T_p	$\overline{\theta^*_{he}}$ (degrees)	$d\sigma / d\Omega$ $\left(10^{-32}\ cm^2/str\right)$
377 MeV	55.5 ± 1.6	51.9 ± 6.5
	65.0 ± 1.8	41.4 ± 4.3
	62.2 ± 1.7	46.8 ± 3.6
	73.0 ± 2.0	41.8 ± 2.8
	83.6 ± 3.1	37.6 ± 2.6
	94.6 ± 3.3	30.6 ± 2.2
462 MeV	56.5 ± 1.3	33.2 ± 2.3
	67.6 ± 1.7	28.9 ± 2.2
	78.7 ± 2.2	30.9 ± 2.6
	70.9 ± 1.8	33.3 ± 2.0
	80.4 ± 2.4	31.4 ± 1.9
	90.0 ± 3.3	27.8 ± 1.7
	99.5 ± 3.1	29.8 ± 1.8
	109.1 ± 2.9	27.9 ± 2.0
	105.4 ± 2.9	35.7 ± 3.9
	113.9 ± 2.8	43.4 ± 4.0
	122.6 ± 2.8	94.4 ± 6.5
	77.5 ± 2.2	34.6 ± 7.0
576 MeV	65.2 ± 1.4	24.0 ± 2.5
	74.7 ± 1.7	24.1 ± 2.5

TABLE 3. Summary of Corrections and Errors (%)

θ^*_{He}	Beam Gate	Dead Time	^{3}He Break-up	χ^2-cut	Accidental Triggers*		Back-ground	Total Correction with Systematic Error	Statist-ical Error
377 MeV					Type(ii)	Type(i)			
55.5°	+2.0±0.4	+14.8±1.5	+2.2±0.6	+4.7±0.9	-6.2±1.2	-2.1±0.4	-5.8±2.3	+9.6±3.2	12.2
65.0	+2.0±0.4	+14.8±1.5	+2.2±0.6	+4.7±0.9	-6.2±1.2	-2.2±0.4	-7.2±1.8	+8.1±2.9	10.1
62.2	+2.0±0.4	+14.8±1.5	+2.2±0.6	+5.3±1.1	-6.5±1.3	-1.9±0.4	-6.4±1.5	+9.5±2.9	7.1
73.0	+2.0±0.4	+14.8±1.5	+2.2±0.6	+5.3±1.1	-6.5±1.3	-1.7±0.3	-7.2±1.6	+8.9±2.9	6.0
83.6	+2.0±0.4	+14.8±1.5	+2.2±0.6	+5.3±1.1	-6.5±1.3	-1.6±0.3	-8.0±1.8	+8.2±3.0	6.1
94.6	+2.0±0.4	+14.8±1.5	+2.2±0.6	+5.3±1.1	-6.5±1.3	-1.7±0.3	-9.8±2.6	+6.3±3.5	6.2
462 MeV									
56.5	+0.9±0.2	+16.9±1.7	+2.2±0.6	+5.7±1.1	-5.3±1.1	-1.8±0.4	-2.5±0.3	+16.1±2.5	6.3
67.6	+0.9±0.2	+16.9±1.7	+2.2±0.6	+5.7±1.1	-5.3±1.1	-1.7±0.3	-3.7±0.4	+15.0±2.5	7.3
78.7	+0.9±0.2	+16.9±1.7	+2.2±0.6	+5.7±1.1	-5.3±1.1	-1.8±0.4	-5.2±0.5	+13.4±2.5	8.1
70.9	+1.8±0.4	+4.6±0.5	+2.2±0.6	+6.1±1.2	-5.7±1.1	-1.7±0.3	-4.5±0.5	+2.8±1.9	5.7
80.4	+1.8±0.4	+4.6±0.5	+2.2±0.6	+6.1±1.2	-5.7±1.1	-1.9±0.4	-6.3±0.6	+0.8±2.0	5.7
90.0	+1.8±0.4	+4.6±0.5	+2.2±0.6	+6.1±1.2	-5.7±1.1	-1.9±0.4	-7.8±0.8	-0.7±2.1	5.8
99.5	+1.8±0.4	+4.6±0.5	+2.2±0.6	+6.1±1.2	-5.7±1.1	-2.1±0.4	-6.7±0.7	+0.2±2.0	5.7
109.1	+1.8±0.4	+4.6±0.5	+2.2±0.6	+6.1±1.2	-5.7±1.1	-2.0±0.4	-6.3±0.6	+0.7±2.0	6.5
105.4	+0.9±0.2	+16.9±1.7	+2.2±0.6	+6.3±1.3	-5.1±1.1	-2.3±0.5	-6.8±0.7	+12.1±2.6	10.6
113.9	+0.9±0.2	+16.9±1.7	+2.2±0.6	+6.3±1.3	-5.1±1.1	-2.5±0.5	-6.6±0.7	+12.1±2.6	8.8
122.6	+0.9±0.2	+16.9±1.7	+2.2±0.6	+6.3±1.3	-5.1±1.1	-2.6±0.5	-6.1±0.6	+12.5±2.6	6.4
2-γ 77.5°	+0.9±0.2	+16.9±1.7	+2.2±0.6		-18.0±3.6			+2.0±4.0	20.3
576 MeV									
65.2	+3.7±0.7	+19.7±2.0	+2.2±0.6	+6.7±1.4	-5.9±1.2	-18.1±3.6	-4.6±0.5	+3.7±4.6	9.2
74.7	+3.7±0.7	+19.7±2.0	+2.2±0.6	+6.7±1.4	-5.9±1.2	-17.9±3.6	-4.6±0.5	+3.9±4.6	9.1

* See page for an explanation of these two types of accidental triggers

0 0 0 4 2 3 0 0 9 7 4

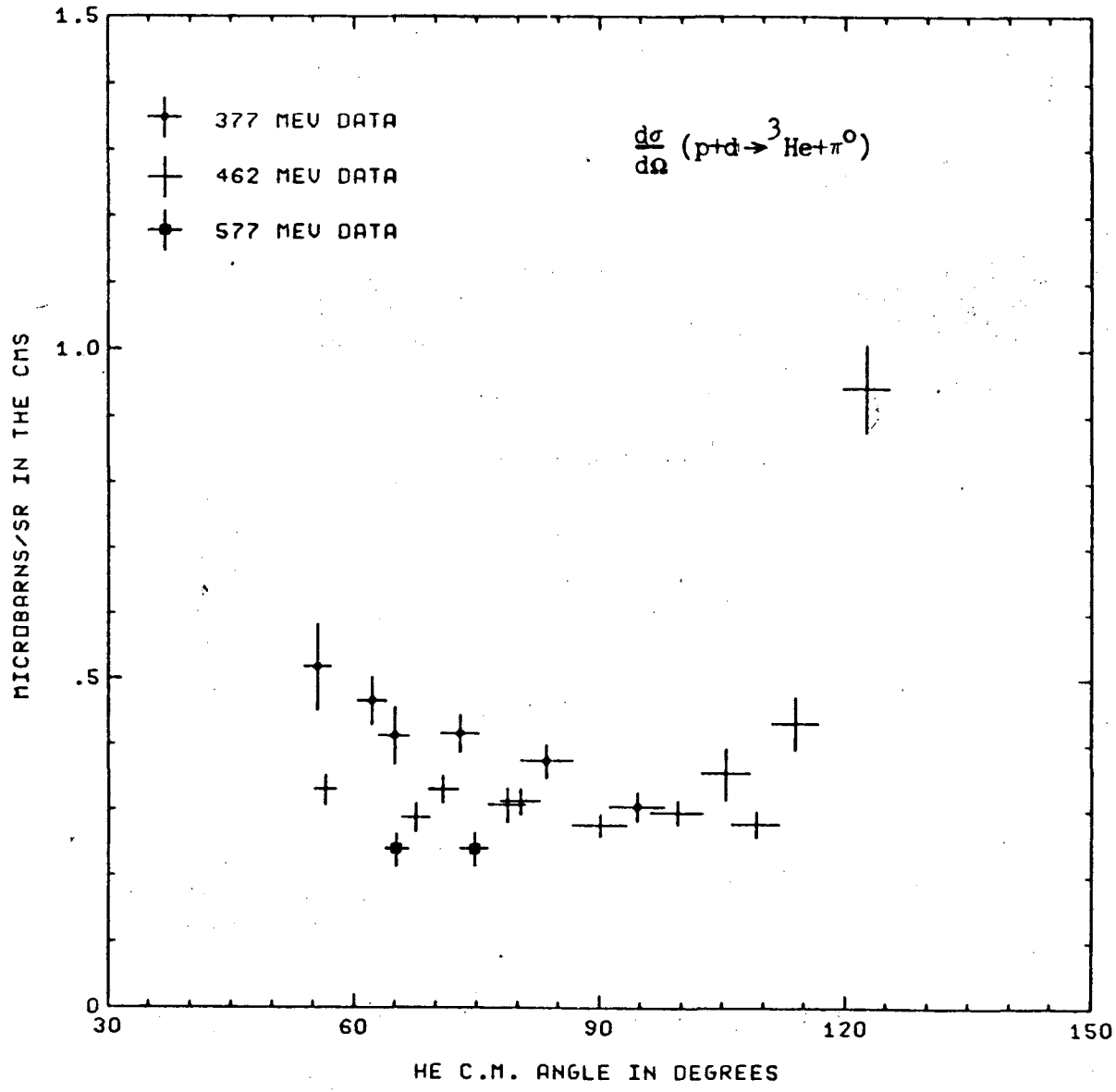

Fig.24 Differential cross-section for the reaction $p+d \rightarrow {}^3He+\pi^0$ at T_p=377, 462, and 576 MeV.

V. DISCUSSION AND CONCLUSIONS

A. Models for Pion Production [44]

The curves in fig. 25 and 26 represent estimates of the cross-section in the two-nucleon approximation. These estimates are based on the work of Barry,[10] specifically on the process represented by the graph shown in fig. 2(b). Assuming that the neutron is on the mass-shell, or equivalently, that it plays the role of a spectator in the sense of the impulse approximation, the dpn and tdn vertex functions Φ can be written as in Ref. (11) as

$$\frac{\Phi_d(p_1^2)}{\sqrt{2M_d}(p_1^2+m^2)} = 2\pi^{\frac{3}{2}}\phi_d^*(\vec{n}-\tfrac{1}{2}\vec{d}) = \int d^3x\,\psi_d^*(x)\exp[i\vec{x}\cdot(\vec{n}-\tfrac{1}{2}\vec{d})], \qquad (1)$$

$$\frac{\Phi_d(p_1^2)}{\sqrt{2M_t}(d_1^2+M_d^2)} = 2\pi^{\frac{3}{2}}\phi_t(\vec{n}-\tfrac{1}{3}\vec{t}) = \int d^3x\,\psi_t(x)\exp[-i\vec{x}\cdot(\vec{n}-\tfrac{1}{3}\vec{t})], \qquad (2)$$

where $\vec{n}$, $\vec{d}$, $\vec{t}$, are the c.m. three-vectors of the neutron, deuteron and triton respectively, and m, M_d, M_t, their respective masses; p_1^2 and d_1^2 represent the squares of the magnitudes of the momentum four-vectors of the internal proton and deuteron respectively and are equal to

$$p_1^2 = (\vec{d} - \vec{n})^2 \;, \qquad d_1^2 = (\vec{t} - \vec{n})^2 \;; \qquad (3)$$

ψ_d and ψ_t denote the spatial wave functions of the initial and final state nuclei with ϕ_d and ϕ_t their momentum-space counterparts.

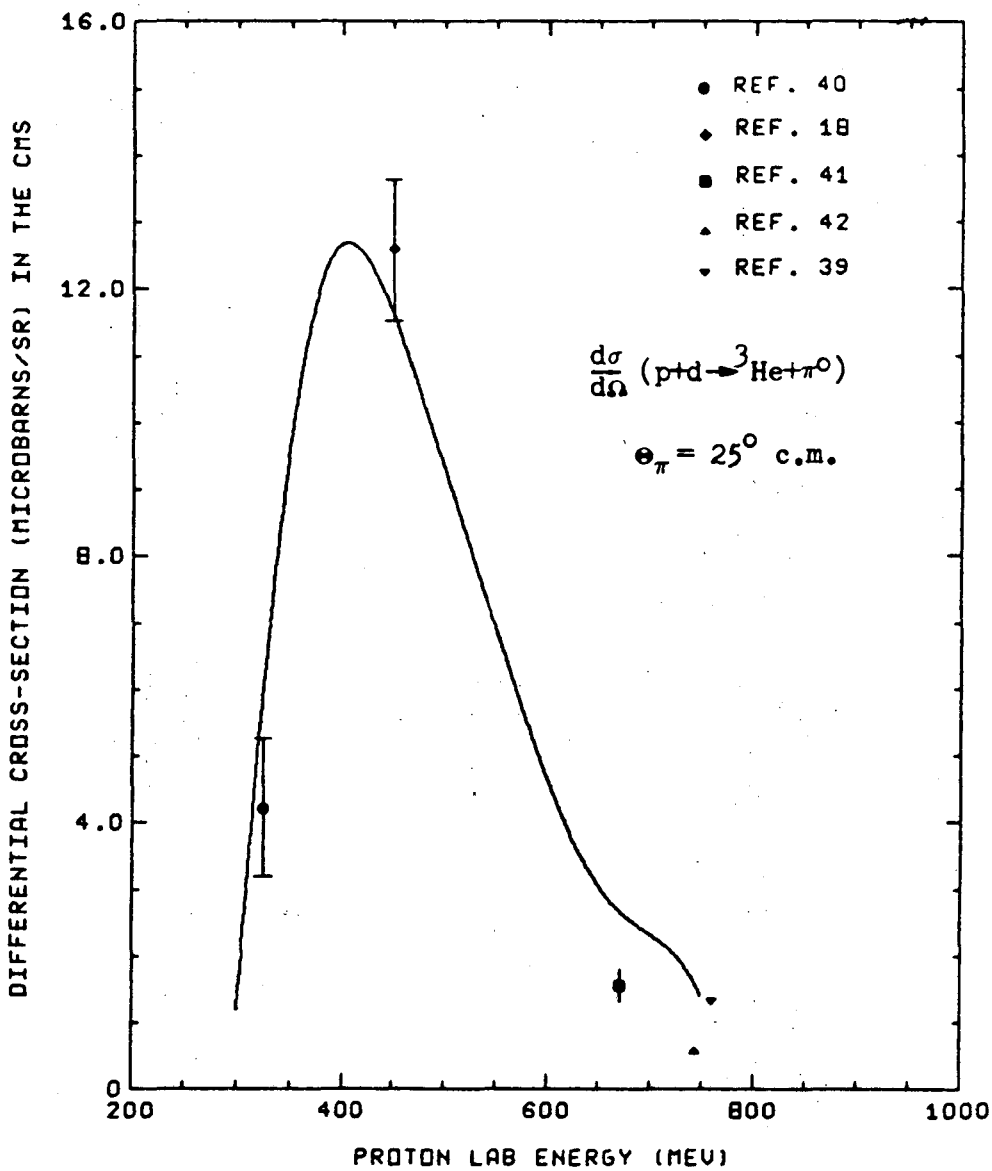

Fig.25 Energy dependence of the differential cross-section for the reaction $p+d \rightarrow {}^3He+\pi^0$ at $\Theta_\pi=25^\circ$. The solid curve represents the prediction of Barry's model (Ref.10) for the process shown in fig.2(b).

0 0 1 4 3 0 0 9 7 6

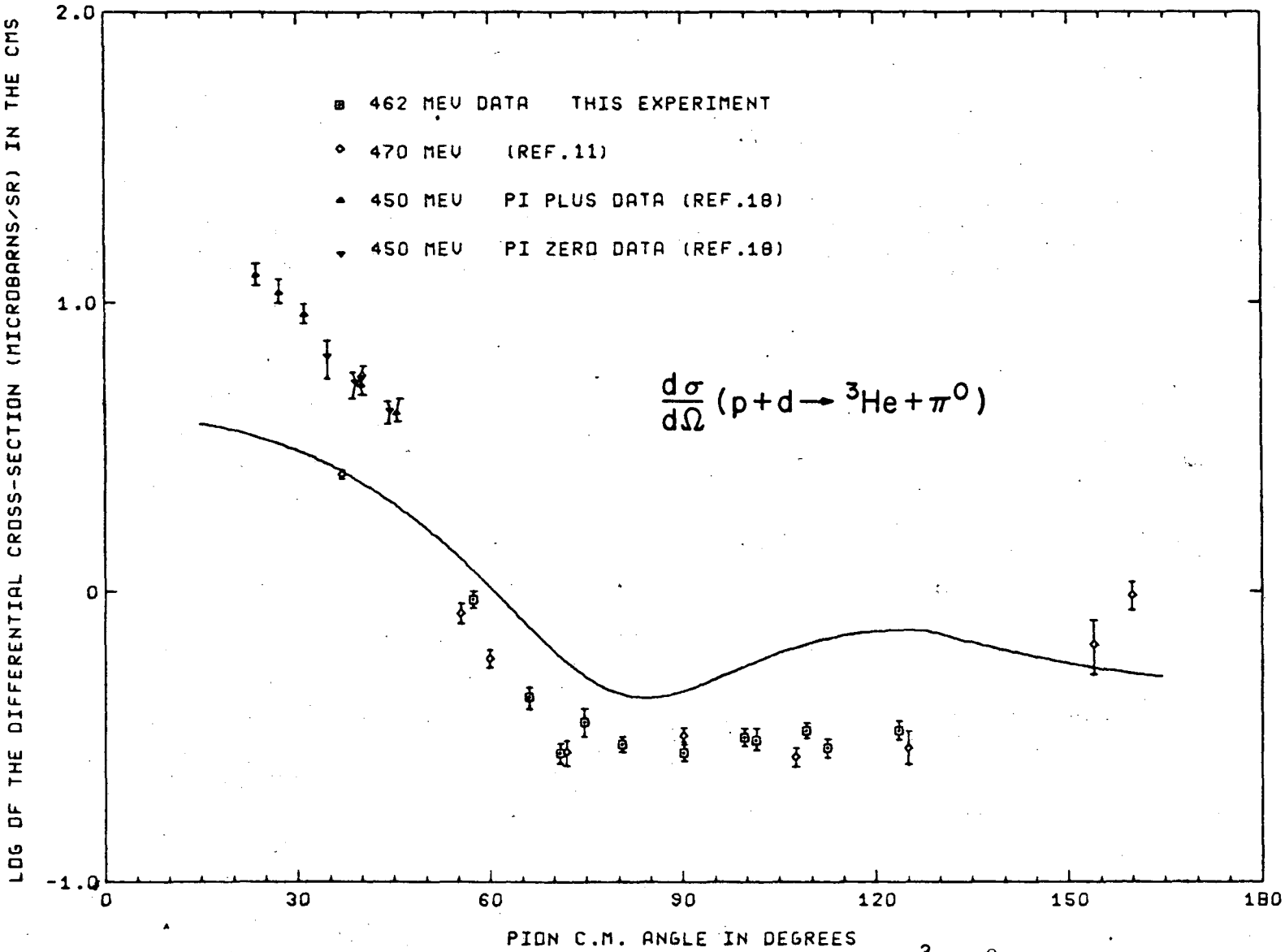

Fig.26 Angular dependence of the cross-section for the reaction $p+d \rightarrow {}^3He+\pi^0$ at T_p=460 MeV. The solid curve is the prediction of Barry's model (Ref.10).

XBL 747-3606

Neglecting spin, the amplitude for the two-nucleon process is

$$\sqrt{M_d M_t}\int \frac{d^3n}{n_o}\, \phi_d^*(\vec{n}-\tfrac{1}{2}\vec{d})\phi_t(\vec{n}-\tfrac{1}{3}\vec{t})T^{pp\to t\pi}(s_{\pi d},u,\vec{n}) \ . \tag{4}$$

Since the function $\phi_d^*\phi_t$ peaks at $\vec{n}\sim\frac{1}{3}\vec{t}$ and $\vec{n}\sim\frac{1}{2}\vec{d}$, whereas the amplitude $T^{pp\to d\pi}$ at the $p(p,\pi)d$ vertex varies only slowly with $\vec{n}$, the amplitude can be reduced to

$$\sqrt{6}G_{dt}^2(\vec{\Delta})T^{pp\to d\pi}(s_{\pi d},u) \ , \tag{5}$$

giving for the reaction $d(p,\pi^+)t$ the cross-section

$$\frac{d\sigma^{\pi t}}{d\Omega} = 6G_{dt}^2(\vec{\Delta})\,\frac{|t_\pi||p_p|}{|d_p||d_\pi|}\,\frac{s_{\pi d}}{s_{\pi t}}\,\frac{d\sigma^{\pi d}}{d\Omega} \ , \tag{6}$$

where $\vec{\Delta}$ is the momentum transfer

$$\tfrac{1}{2}\vec{d} - \tfrac{1}{3}\vec{t} \ , \tag{7}$$

$G_{dt}(\vec{\Delta})$ is the form factor

$$G_{dt}(\vec{\Delta}) = \int d^3x\,\psi_d^*(x)\psi_t(x)\exp(-i\vec{x}\cdot\vec{\Delta}) \ , \tag{8}$$

$|t_\pi|$ and $|d_p|$ the magnitudes of the triton and deuteron c.m. three-momenta respectively in the reaction $d(p,\pi^+)t$, with $|d_\pi|$ and $|p_p|$ the corresponding quantities for the reaction $p(p,\pi^+)d$. Cross-section data for the reaction $p(p,\pi^+)d$ are taken from the article cited in Ref. (4).

The relation between the c.m. energies for the two reactions is somewhat ambiguous. If the intermediate deuteron in fig. 2(b) is assumed to be on the mass shell ($\vec{n}\sim\frac{1}{3}\vec{t}$), one gets for the relation between

the invariant energies squared, s, for the πd and πt processes

$$s_{\pi t} = \frac{3}{2} s_{\pi d} + 3m^2 - \tfrac{1}{2}m_\pi^2 , \tag{9}$$

If the proton is assumed to lie on the mass shell ($\vec{n} \sim \frac{1}{2}\vec{d}$), the result is

$$s_{\pi t} = 2s_{\pi d} + m^2 , \tag{10}$$

where m is the nucleon rest mass and m_π the pion rest mass. Experimental evidence[6] indicates that the (3,3) resonance bump in the $t\pi$ data is near a laboratory proton energy of 450 MeV, which is in agreement with the prediction of Eq. (9). According to Eq. (10), on the other hand, a bump would be expected near 600 MeV. The relation (9) is adopted as the more reasonable of the two, at least near 450 MeV, and is used in what follows.

Another ambiguity arises in relating the scattering angles for the two processes since the model involves the $p(p,\pi)d$ reaction with one nucleon (p_1) off the mass shell. Two natural ways of resolving this difficulty are discussed in Ref. (45) and the prescription in which the momentum transfers are equated (u-fixed prescription) is chosen as the more reasonable.

Barry (Ref. 10) points out that an additional ambiguity is associated with the fact that $\vec{\Delta}$, as defined in Eq. (7), is not a relativistic invariant. This difficulty is overcome by constructing quantities which depend on $\vec{\Delta}$ but are relativistically invariant and then choosing the most reasonable prescription based on empirical grounds. In what follows, the relation

$$\Delta_b^2 = \Delta^2 - \Delta_{min}^2 \tag{11}$$

is used since this value gives a reasonably good fit[10] to the form factor, G_{dt}

Gaussian wave functions

$$\psi_d(x) = \left(\frac{\beta_d^2}{\pi}\right)^{3/4} \exp(-\tfrac{1}{2}\beta_d^2 x^2) , \tag{12}$$

$$\psi_t(x) = k_t^{1/2} \left(\frac{\beta_t^2}{\pi}\right)^{3/4} \exp(-\tfrac{1}{2}\beta_t^2 x^2) , \tag{13}$$

where β_d = 87 MeV, β_t = 106 MeV (Ref. 10), are used in calculating G_{dt}. $\psi_t(x)$ is the d-n component of the triton wave function, and k_t is expected to be 1/2,[31] and this is assumed in the present calculation (although this may not be an accurate representation according to Ref. 32).

The value of $\psi_t(0)$ needed to fit the data of fig. 25 is a factor of $\sqrt{4.3}$ lower than that suggested by the Gaussian form of Eq. (13). In fig. 26 the same factor is used. The fit to the energy dependence is respectable. Agreement in the case of the angular distribution is very poor, even at small angles where the two-nucleon approximation is expected to be valid and where contributions from the graphs in fig. 3 and 4 are at a minimum. Neither the use of different wave functions nor recourse to other methods of resolving the ambiguities mentioned above significantly improve the small angle fit. The small angle fits shown in Ref. (11), for example, are much worse if the data of Crewe et al.[18] at 450 MeV are included. It must be emphasized, however, that this model does not include the graphs of fig. 2(a) and (c). The latter is expected to be relatively unimportant (see p. 1447, Ref. 10). But the same cannot be said for the former. The problem here is that there

is no good relativistic model for the off-shell π - d - (pp) vertex.

In the backward direction, i.e., θ_π close to 180°, the one-pion exchange (OPE) graph shown in fig. 3 is expected to be dominant.[10] In this case the cross-section can be written in terms of the π-d elastic scattering cross section,

$$\frac{d\sigma^{\pi t}}{d\Omega} = \tfrac{1}{2}G^2_{pt}(k_1^2)\left|\frac{t_\pi}{P_d}\right| \frac{s_{\pi d}}{s_{\pi t}} \frac{d\sigma^{\pi d \to \pi d}}{d\Omega} \quad , \tag{14}$$

where

$$s_{\pi t} = \tfrac{3}{2}\, s_{\pi d} + 3m^2 - \tfrac{1}{2}\mu^2 \ ,$$

$$k_1^{\ 2} = \tfrac{1}{3}[4m^2 + (t-p)^2] \ ,$$

The form factor $G_{pt}(k_1^2)$ is given by

$$G_{pt}(k_1^2) = \psi_t(0)\ \sqrt{6}GF(k_1^2)k_1/\sqrt{m}(k_1^2 + m_\pi^2) \ , \tag{15}$$

where $G^2/4\pi = 14.7$, $F(k_1^{\ 2}) = \left(1 + \dfrac{k_1^{\ 2} + \mu^2}{60\mu^2}\right)^{-1}$.

The parameters used in the tritium wave-function are the same as those used above. The π-d elastic scattering data were adapted from Refs. 33-38. The 180° cross-section data are shown in fig. 27, with the curve indicating the prediction given by Eq. (14). The value of $\psi_t(0)$ needed to fit the data is a factor of $\sqrt{5.9}$ smaller than that suggested by the Gaussian form of Eq. (13). Qualitatively, the features of the data are faithfully reproduced. In particular, the bumps at about 1.05 GeV coincide quite well although the preceding trough is somewhat washed out

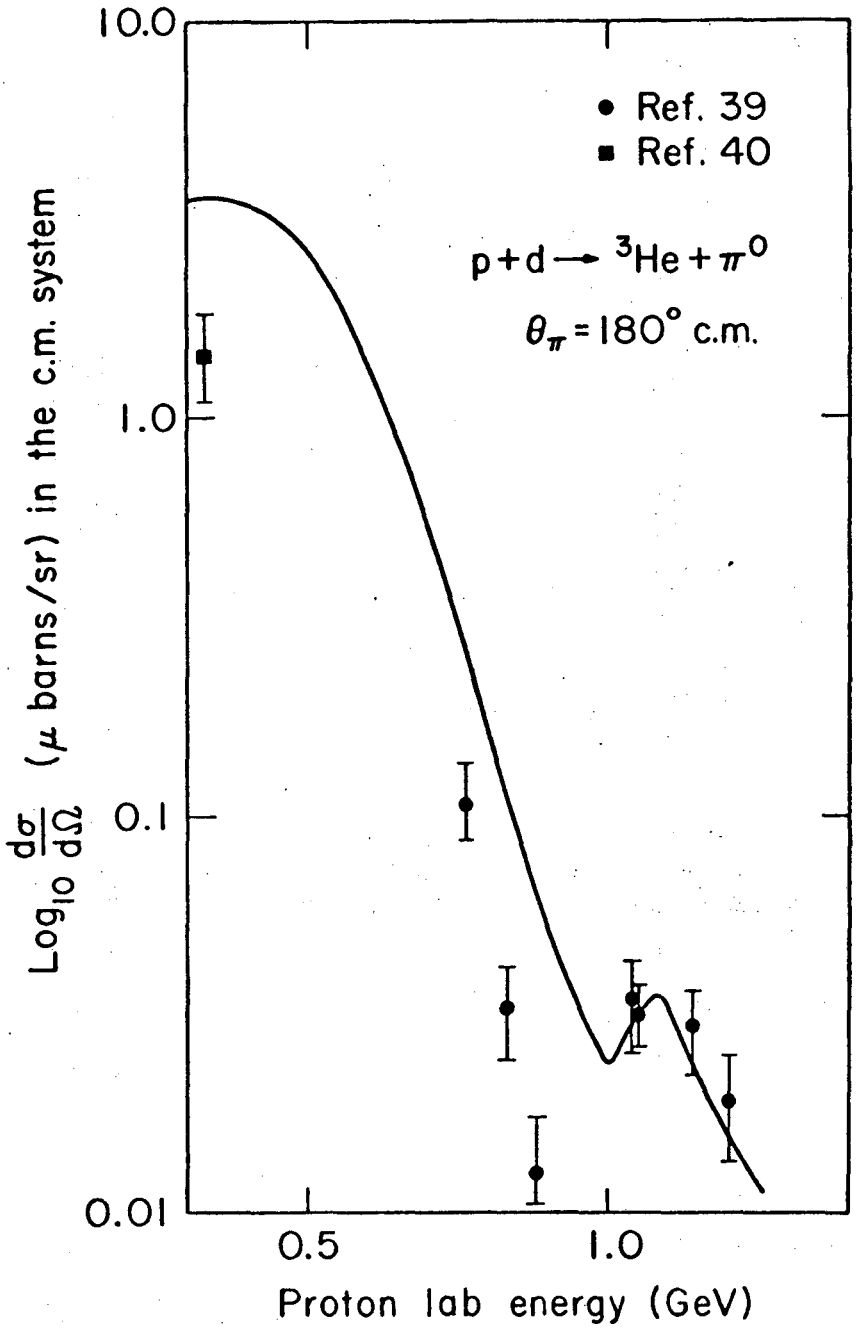

Fig.27 Energy dependence of the differential cross-section for the reaction $p+d \rightarrow {}^3He+\pi^0$ at $\theta_\pi=180°$. The solid curve represents the prediction of Barry's model (Ref.10) for the process shown in fig.3.

in the theoretical curve. This bump reflects the bump at T_π=580 MeV in the 180° πd elastic scattering cross-section, and it is believed to be due to excitation of the N*(1540).[10]

A serious deficiency of this model, as pointed out by Dollhopf et al.[11] is its inability to reproduce the backward peak in the angular distribution. This rise in cross-section at large angles can be seen in fig. 26. Similar behavior is apparent in the 377 MeV data of this experiment (fig. 24) and in the data of Chapman et al.[40] at 325 MeV. The OPE model for backward scattering predicts a flat angular distribution like πd elastic scattering near 180°. Inclusion of the single-nucleon process in the model does not help. This process, represented by the graphs shown in fig. 4, involves very large internal momenta and consequently its contribution is relatively insignificant with respect to that of the OPE process. In the graph of fig. 4(a) the incoming proton emits a pion and the resulting neutron is subsequently captured by the target. This process favors forward pion emission and the internal nucleon momentum involved is $|\vec{\Delta}| = |\vec{p} + \frac{2}{3}\vec{t}|$. For an incident proton energy of 470 MeV, this gives an internal momentum of 815 MeV/c for backward pion emission. In the graph of fig. 4(b) it is the target which emits the pion and then captures the incoming proton to form a bound triton. In this case the internal momentum is given by $|\vec{\Delta}| = |\vec{p} - \frac{1}{3}\vec{t}|$ and backward pion emission is favored, for which $|\vec{\Delta}|$ = 550 MeV/c at 470 MeV beam energy. Although this is not as large as in the first process it is still a very large momentum on a scale of internal nuclear momenta.

In conclusion, none of the processes discussed above appear to explain the backward peak nor the sharpness of the forward peak. The two-nucleon model and the OPE model do however reproduce the features of the energy dependence of the cross-section for forward and backward pion emission respectively. Before meaningful information about the deuteron and triton can be extracted, the theoretical situation must be clarified. Further work directed at including the OPE graph shown in fig. 2(a) in the model would be helpful in resolving the discrepancy with the forward peak. This graph can certainly not be neglected a priori. As for the problem of the backward peak, it appears that additional reaction mechanisms will have to be considered. A systematic experimental study of the angular distribution of the reaction $pd \rightarrow t\pi^+$ (or $^3He\pi^o$) in the energy region 300 - 600 MeV will further these ends.

B. Isotopic Spin Invariance

Using the recent data of Dollhopf et al.[11] at 470 MeV, the ratio $R=\sigma(^3H\pi^+)/(^3He\pi^o)$ can be calculated over a fairly wide angular region. Since the precision obtained in the measurements of this ratio (10 - 20%) is much larger than the Coulomb and mass corrections and the corrections for the different c.m. energies (2 - 3%; see Appendix D), these corrections are ignored and the value R=2.0 is used in comparing the data shown in fig. 26. In the numerical summary given in Table 4, however, these minor corrections are included.

At some angles, especially for the smaller pion angles, this ratio is more than one standard deviation below the theoretical value, but this discrepancy may well be attributed to the estimated 15% systematic

TABLE 4

Isospin Comparison

θ_π (degrees)	Differential Cross-Section (μb/sr)		R_{exp}	R_{th}
	$t\pi^+$; T_p=470 MeV	$^3He\pi^0$; T_p=462 MeV		
55.5	1.69 ± 0.13*	1.15 ± 0.25	1.47 ± 0.35	2.01 ± 0.07
60.0	1.17 ± 0.08	0.74 ± 0.16	1.58 ± 0.35	2.02 ± 0.07
72.0	0.55 ± 0.06	0.28 ± 0.02	1.96 ± 0.26	2.03 ± 0.07
90.0	0.63 ± 0.06	0.30 ± 0.02	2.10 ± 0.26	2.04 ± 0.07
107.5	0.54 ± 0.05	0.32 ± 0.02	1.69 ± 0.21	2.05 ± 0.07
125.0	0.58 ± 0.08	0.31 ± 0.02	1.87 ± 0.28	2.05 ± 0.07

* There is also a systematic error on the order of 15% associated with these data (p.390, Ref.11) which has not been taken into account here.

0 0 0 4 3 0 0 9 8 0

error in the $(^3H, \pi^+)$ data which was not considered in calculating the ratio. There is also a quite serious disagreement between the data of Dollhopf et al. and the data of Crewe et al.[18] near $\theta_\pi = 35°$. This further suggests that the former data are systematically low for small pion angles.

It is concluded that the agreement with isospin invariance is satisfactory when systematic errors are taken into account, except at small pion angles where the $^3H\pi^+$ data seems to be systematically low.

0 0 0 4 3 0 0 9 8 1

Acknowledgements

I am indebted to many people for the successful completion of this experiment.

I am grateful to my research advisor, Professor Victor Perez-Mendez, for his support and guidance during the course of the experiment.

I greatly appreciate the help and advice of Professor Clem Heusch, Drs. Jim Carroll, Michael Goitein, Robert Klein, Burns Macdonald, and Al Stetz throughout the experiment. I am particularly indebted to Drs. Carroll and Goitein for their patient and invaluable assistance during the analysis phase of the experiment.

I would like to thank Karl Stein for his technical support during the experiment, the 184-inch cyclotron crew for their excellent service, and Jeanne Elliott for carefully typing this manuscript.

Appendix A: Beam Energy Calibration

The energy of the incident proton beam was calibrated to determine the absolute energy of the interacting proton for a given event. To assign an energy to a given event it is necessary to a) assign an average energy to all incident protons, and b) to correct that value based on the characteristics of the event. The only significant parameter in the correction (b) is the horizontal displacement of the event vertex from the average position of all events. Other parameters, such as the angle at which the proton enters the target, and depth of the interaction in the target are relevant but not particularly susceptible to measurement.

First will be discussed the estimate of the average energy of all protons at a point half-way through the liquid target for a given run. This number is based on the nearest range measurement, with corrections made for any change in the excitations of the two magnets at Bend 1 and Bend 2 (see fig. 6). The second part of the following discussion will be concerned with corrections to this energy on an event-by-event basis.

Range-Energy tables, such as Janni's,[46] are based on parameters derived largely from low energy measurements and must be considered suspect at energies in the range of interest of this experiment. (The assumption of the velocity independence of the ionizing potential is particularly weak.) The absolute range-energy calibration, therefore, has been based on two experiments[21,22] which bracket the energy range of interest. The stated accuracies of the measurements are about

± 1/3% in energy. The ratio of the energies observed to those which would be predicted by Janni's tables as giving the same range are:

$$T_2/T_J = 1/.9949 \ ,$$

$$T_3/T_J = 1/.9964 \ ,$$

where T_2 and T_3 are the observed energies in ref. 21 and 22, respectively, and T_J is that proton energy in Janni's table which gives the same range. Janni's tables were used as a suitable way of interpolating energies from measured ranges, but the interpolated energies are raised by a normalization factor of 1.0044 (which is the average of 0.9949^{-1} and 0.9964^{-1}). Janni's tables (protons in Cu) were fit by the formula:

$$\begin{aligned} LOG_e T(MeV) = \ & 3.2273 + 0.53471 \left[LOG_e R \ (g/cm^2)\right] \\ & + 0.016216 \ (LOG_e R)^2 \\ & - 3.6318 \times 10^{-3} \ (LOG_e R)^3 \\ & + 4.3731 \times 10^{-4} \ (LOG_e R)^4 \end{aligned}$$

In deducing the energy from the range it is necessary to know the thickness of the various elements of the absorber. The energy of the proton beam, upon exiting from the first ion chamber (see fig. 7), was based on careful measurements of the material between it and the center of the second ion chamber. This energy was reduced by 0.24 MeV to obtain the average proton energy at the center of the 1/2-inch liquid deuterium target.

Given the average proton beam energy for a particular run, an energy is assigned to each interacting proton. As described in section II.B.2, the momentum dispersion across the target was approximately 0.4% per inch. The proton energy for a given event is then

$$T_{event} = T_{ave} \left[1 + 0.004 \left| \frac{PdT}{Tdp} \right| (y-y_o) \right]$$

where .004 is the average of the measured and theoretical dispersions (see II.B.2), $\left| \frac{PdT}{TdP} \right|$ is $\frac{1}{.597}$ at T = 460 MeV, y is the horizontal event coordinate (positive to the left looking downstream), y_o is the average horizontal event coordinate for the run considered, and T_{ave} is the average beam energy for the run. Both y and y_o are determined by track reconstruction from the He chambers.

Appendix B: Ionization Chamber Calibration

In order to directly count protons in a beam, it is essential that the proton current be at a level low enough so that counting losses are not beyond correction. On the other hand, the proton current must be high enough so that losses due to leakage current in the ionization chamber and losses in the integration device are not beyond correction. This constraint is difficult to satisfy. One method of circumventing the problem is to use an intermediate scaling device that is reliable at both the low proton current, where the direct proton counting is performed, and at high current, where the ionization chamber is reliable.

In this calibration, elastic p-p scattering was used as the scaling device. The important parts of the apparatus are shown in fig. 8. The direct proton counters (DPC) consisted of three circular (12-in. diameter, 1/8-in. thick) Pilot-B scintillators in coincidence. A CH_2 target (4-in. thick) was used for the p-p scattering. The detectors were scintillator telescopes.[47] The ionization chamber was filled with He and was partitioned into four regions by five 1 mil Al foils. The central foil served as the collector, and the adjacent foil on either side was at high voltage.

The proton scattering angle of 42° (90° cm for 558 MeV protons) was chosen since the differential cross section is flat at this angle. Hence, counting losses due to variations in beam steering are minimized with this geometry. The effect of beam missteering on the p-p scattering rate was about 0.4% for the maximum beam displacement during a

typical run. This maximum occurred less than 1% of the time so corrections due to beam steering can be neglected.

The validity of the calibration is based on two premises: first, that there is a one-to-one correspondence between protons incident on the ionization chamber and counts from the coincidence circuit; second, that counting losses in the scaling device are directly proportional to the proton beam rate.

Three factors challenge the validity of the first assumption: scattering, dead time losses, and coincidence inefficiencies. Protons can scatter in the ionization chamber (IC) and deplete the beam at the DPC. This scattering is of two types: nuclear and Coulomb. Nuclear absorption in the IC amounts to at most a 0.05% loss. Coulomb scattering is even less significant. Absorption losses in the DPC themselves are more important. The calculated absorption loss in a 1/8-in. plastic scintillator is 0.6%. Measurement, however, indicated a 0.4% discrepancy[48] between a three-fold coincidence and a coincidence requiring any two of the three counters. This implies a 0.133% absorption inefficiency for each counter. This discrepancy (0.133% vs 0.6%) is probably due at least in part to the detection of charged debris in the downstream counter(s). A correction of 0.4% with an uncertainty of 0.1%, was made for absorption in the DPC.

Dead time losses result from the finite response time of the coincidence and scaling circuitry. In our case, a counting rate of 20 MHz was imposed by the scalers. Synchrocyclotron beams are divided into microstructure bursts having the rf acceleration frequency and a

width of a few nsec (about 7 nsec in our case), generally less than one counting resolution. Consequently, only one pulse can be counted per rf period, and "losses" arise because the scaler is unable to detect whether only one, or more than one, proton is present in a microstructure burst. Using Poisson statistics, one can estimate the loss. If m is the mean number of protons per burst in a steady beam, and its value is small, the fraction of protons which occur in such multiple-proton bursts is about m/2. For a time average beam rate of 10^5 protons/sec, the rate in the microstructure burst is about 10^6 protons/sec because of the 10% macroburst duty factor of the 184-in. synchrocyclotron. Since the burst width is 7 nsec, $m = 10^6$ protons/sec $\times$ 7 nsec/burst $= 7 \times 10^{-3}$ protons/burst. So the percentage of protons occuring in multiproton bursts is about 0.35%. A more rigorous treatment of dead time losses is given by Cormack[49] for the following values of the parameters:

τ = 50 ns dead time

T = 7 ns microburst width

t_o = 52 ns rf period

λ_1 = 10^5/sec average proton beam rate.

Agreement between these two numbers is respectable. A dead time correction was made for the DPC rate based on the 0.3% figure. An uncertainty of 20% was assigned to this correction.

This efficiency of the coincidence circuit was affected by two main factors: accidental coincidences and coincidence inefficiency due

to timing jitter. The accidental rate was determined by delaying one counter of the three DPC by one rf period. From this a three counter accidental rate of about 0.06% was calculated. Inefficiency due to timing jitter was less than 0.01%. Both these effects are small and were neglected.

Only one factor challenges the validity of the second premise: accidental coincidences. Losses due to scattering, dead time, and coincidence inefficiency are all directly proportional to beam rate and hence cancel out between the low and high beam rate measurements. The accidental coincidence rates in the proton telescopes were measured and corrected for. The rate was never more than 5%, and typically about 2%.

During the high beam rate measurement, the DPC remained in the beam so that the convenient cancellation of beam rate proportional losses in the scaling device remained valid. Drift current in the IC was typically 0.7 pA. This amounted to about 0.5% of the measured current and was corrected for. A unit of charge in the integrator used is defined for convenience as an "Ort", and a coincidence between the two proton telescopes is called a "mon".

One IC calibration was made at each of two proton beam energies: 558 MeV and 462 MeV (with the appropriate changes in proton telescope angles and absorber).

At 558 MeV:

Low Beam Rate $\quad$ mon/DPC = $99.2 \pm 1.6/10^7$ protons

The error is dominated by the statistical error of the DPC counts.

High Beam Rate $\quad$ mon/Ort = 305.1 ± 0.6 ,

so protons/Ort = $3.08 \pm 0.05 \times 10^7$.

At 462 MeV:

Low Beam: 110 ± 2 mon/10^7 protons

High Beam: mon/Ort = 314.5 ± 1.5,

so protons/Ort = $2.86 \pm 0.05 \times 10^7$.

For comparison, the 558 MeV calibration is corrected for the rate of energy loss in the ionization chamber to correspond to the 462 MeV calibration:

$$\text{protons/Ort (462 MeV)} = \text{protons/Ort (558 MeV)} \times \left.\frac{dT}{dx}\right|_{he} (T_p = 558 \text{ MeV}) / \left.\frac{dT}{dx}\right|_{he} (T = 462 \text{ MeV})$$

$$= 3.08 \times 2.51/2.72 = 2.84 \pm 0.05 \times 10^7 .$$

Appendix C: Least-Squares Kinematic Fitting

Minimizing a Chi-squared value subject to non-linear constraints is treated in detail elsewhere.[29] Therefore, only the general techniques will be sketched below.

In general the procedure consists of having a set of n measured variables (X_i^m , i = 1, ... , n), estimates of the measurement errors (ΔX_i^m), and a set of constraining equations

$$F_K(X) = 0 , \qquad K = 1, \ldots , C , \tag{1}$$

where $X = (X_1 , X_2 , \ldots , X_n)$.

The error matrix, taken to be diagonal in this experiment, is defined as

$$G_{ij}^{-1} = \Delta X_i^m \quad \Delta X_j^m \quad \delta_{ij} \tag{2}$$

The quantity to be minimized, subject to the constraint equations (1), is defined as:

$$\chi^2 = \sum_{i,j=1}^{n} (X_i - X_i^m) G_{ij}(X_j - X_j^m) \tag{3}$$

This is done by introducing lagrange multipliers, α_K , and minimizing

$$M = \chi^2 + 2 \sum_{K=1}^{c} \alpha_K F_K(X) . \tag{4}$$

The conditions for minimizations are

$$\frac{\partial M}{\partial X_i} = 2 \left[\sum_{j=1}^{n} G_{ij}(X_j - X_j^m) + 2 \sum_{K=1}^{c} \alpha_K \frac{\partial F_K}{\partial X_i} \right] = 0 \quad (5a)$$

and

$$\frac{\partial M}{\partial \alpha_K} = 2\, F_K(X) = 0. \quad (5b)$$

These equations are, as a rule, non-linear, and their solution in the general case is quite difficult. The problem can be considerably simplified if the constraint equations are sufficiently linear to allow an expansion of low order about a trial solution, $\overline{X}$. To first order equation (5b) is now:

$$F_K(X) = F_K(\overline{X}) + \sum_{i=1}^{n} \frac{\partial F_K}{\partial X_i} \bigg|_{\overline{X}} (\overline{X}_i - X_i) \quad (6)$$

or

$$F_K(X) = F_K(\overline{X}) + \sum_{i=1}^{n} B_{Ki}(\overline{X}_i - X_i)$$

where

$$B_{Ki} = \frac{\partial F_K}{\partial X_i} \bigg|_{\overline{X}}$$

one can then write

$$H_{KW} = \sum_{s=1}^{n} \sum_{t=1}^{n} (\tilde{B})_{KS}\, G^{-1}_{st}\, B_{tw}$$

where $\tilde{B} = B^{\text{transpose}}$.

Then

$$\alpha_K = \sum_{w=1}^{c} (H)^{-1}_{kw} \left[F_k + \sum_{j=1}^{n} (X_j^m - X_j) B_{jk} \right]$$

and,

$$X_i = X_i^m - \sum_{k=1}^{c} \sum_{j=1}^{n} G^{-1}_{ij} B_{jk} \alpha_k .$$

Using these values of the X_i, one determines whether the $F_k = 0$. In practice one sets a tolerance on how well the constraint equations are satisfied. If the tolerance is not satisfied, one uses the new value of X as the new $\overline{X}$ and reiterates the calculation.

Appendix D: Electromagnetic Corrections to Isospin Invariance

As discussed previously, the ratio $R = d\sigma(p+d \rightarrow {}^3H+\pi^+)/d\sigma(p+d \rightarrow {}^3He+\pi^0)$ is equal to 2 according to the isospin formalism when electromagnetic effects are neglected. Köhler[20] has investigated the problem of correcting for these effects and discusses four non-negligible corrections for incident protons of an energy of 600 MeV:

1. a correction based on the difference in the ^3H and ^3He wave functions (effects of Coulomb forces and other differences);
2. a correction resulting from the fact that the two reactions should be compared for the same momenta of the outgoing pions;
3. a correction due to a difference in phase-space factors;
4. a correction for the fact that the pions come out at slightly different c.m. angles.

The first correction is the most important. At 460 MeV beam energy it is typically +2%. Since this correction depends on the particular wave functions used for the triton and ^3He particle, it is somewhat uncertain and Köhler consequently assigns an error of 3% to it. The assumption that the two reactions should be compared at c.m. energies corresponding to equal momenta for the outgoing pions is plausible though disputable. In any case the correction is small. The π^0 and π^+ c.m. momenta are equal when the respective proton lab energies are 462 and 467 MeV. The cross-section increases by 2 ± 1% for a 10 MeV decrease in lab proton energy at $\theta_\pi = 115°$ in the c.m. system and this number is only weakly angle-dependent (cf. -3 ± 1%/10 MeV at $\theta_\pi = 25°$). The

resulting increase in R is about 0.6%. The correction for the difference in phase space factors is typically -0.7%. Finally, the correction for different c.m. angles is negligible. The total correction to R is about 2% and is given angle-by-angle in Table 4. Since this is a small correction, the value R=2 was used for convenience in converting π^+ cross-section data to π^0 data in the graphs of figs. 25 and 26.

References

1. R. V. Kline, Ph.D. Thesis, California Institute of Technology, Pasadena, California (1973).
2. A. M. L. Messiah, Phys. Rev. 86, 430 (1952).
3. M. Ruderman, Phys. Rev. 87, 383 (1952).
4. For a recent experimental study and references to others see C. Richard-Serre et al., Nucl. Phys. B20, 413 (1970). For a recent theoretical study see Ref. (45) below.
5. Ruderman specifically investigated the reaction $p+d \rightarrow {}^3H+\pi^+$ (Ref.3).
6. C. H. Q. Ingram, N. W. Tanner, J. J. Domingo, Nucl Phys. B31, 331 (1971).
7. J. Letourneux and Y. R. Waghmare, Nucl. Phys. 87, 331 (1966).
8. S. A. Bludman, Phys. Rev. 94, 1722 (1954).
9. W. J. Frank, K. G. Bandtel, R. Madey, and B. J. Moyer, Phys. Rev. 94, 1716 (1954).
10. G. W. Barray, Phys. Rev. 7D, 1441 (1973).
11. W. Dollhopf, C. Lunke, C. F. Perdrisat, W. K. Roberts, P. Kitching, W. C. Olsen, J. R. Priest, Nucl. Phys. A217, 381 (1973).
12. B. Cassin and E. U. Condon, Phys. Rev. 50, 846 (1936).
13. N. Kemmer, Proc. Camb. Phil. Soc. 34, 354 (1938).
14. J. Cerny, Ann. Rev. of Nucl. Sci. 18, 27 (1968).
15. J. A. Poirier and M. Pripstein, Phys. Rev. 130, 1171 (1963).
16. K. R. Greider, Phys. Rev. 122, 1919 (1961).
17. B. Schrock, UCLRL 19350 (1969).

18. A. V. Crewe, B. Ledley, E. Lillethun, S. M. Marcowitz, and C. Rey, Phys. Rev. 118, 1091 (1960).

19. D. Harting, J. C. Kluyver, A. Kusumegi, R. Rigopoulos, A. M. Sachs, G. Tibell, G. Vanderhaeghe, and G. Weber, Phys. Rev. 119, 1716 (1960).

20. H. S. Köhler, Phys. Rev. 118, 1345 (1960).

21. R. Mather and E. Segré, Phys. Rev. 84, 191 (1951).

22. V. P. Zrelov and G. D. Stoletov, Soviet Physics JETP 9, 461 (1959).

23. R. J. Tapper, Tables of Vapor Pressure and Molar Volume for Liquid Hydrogen and Deuterium, NIRL/R/95 (1965).

24. Blue Print No. 15P787.

25. The greatest non-uniformity was 10% with respect to the response at the center of the counter. This maximum non-uniformity occurred at the end of the scintillator closer to the phototubes.

26. D. H. Fredrickson, J. B. Carroll, M. B. Goitein, R. V. Kline, B. Macdonald, V. Perez-Mendez, and A. W. Stetz, Nucl. Instr. and Methods 107, 205 (1973).

27. C. A. Heusch, R. V. Kline, C. Y. Prescott, S. J. Yellin, A Hodoscope/Spectrometer for High-Energy Photons, Proceedings of the International Conference on Instrumentation in High Energy Physics, Dubna, USSR, 1970, Vol. 1, p. 419.

28. B. Rust, W. R. Burrus, and C. Schneeberger, ACM 9, 381 (1965).

29. J. Berge, UCID-1252, University of California, Berkeley, California (1960).

30. G. Källén, Elementary Particle Physics, Addison-Wesley Publishing Co., Inc., Palo Alto, 1964, p. 30.

31. L. I. Schiff, Phys. Rev. 133, B802 (1964).

32. Physics Today 27, No. 5, 20 (1974).

33. A. M. Sachs, H. Winick, and B. A. Wooten, Phys. Rev. 109, 1733 (1958).

34. K. C. Rogers and L. M. Lederman, Phys. Rev. 105, 247 (1957).

35. E. G. Pewitt et al., Phys. Rev. 131, 1826 (1963).

36. J. H. Norem, Nucl. Phys. B33, 512 (1971).

37. L. S. Dul'kova, I. B. Sokolova, and M. G. Shafranova, ZH. Eksp. Teor. Fiz. 35, 313 (1959) [Sov. Phys. JETP 8, 217 (1959)].

38. L. S. Schroeder et al., Phys. Rev. Letters 27, 1813 (1971).

39. J. Banaigs, J. Berger, L. Goldzahl, T. Risser, L. Vu-Hai, M. Cottereau, C. Le Brun, Phys. Lett. 45B, 394 (1973).

40. K. R. Chapman, J. D. Jafar, G. Martelli, T. J. MacMahon, H. B. Van Der Raay, D. H. Reading, R. Rubenstein, K. Ruddick, and D. G. Ryan, Nuclear Physics 57, 499 (1964).

41. Yu. K. Akimov, O. V. Savchenko, and L. M. Soroko, ZH. Eksp. Teor. Fiz. 38, 643 (1960) [Sov. Phys. JETP 11, 462 (1960)].

42. N. E. Booth, Phys. Rev. 132, 2305 (1963).

43. A. C. Melissinos and C. Dahanayake, Phys. Rev. 159, 1210 (1967).

44. The models are presented in terms of the $t\pi^+$ final state for convenience. The figures refer to the $^3He\pi^0$ final state. The two cross-sections are related by a factor of 2 according to the isospin prescription.

45. G. W. Barry, Ann. Phys. 73, 482 (1972).

46. J. F. Janni, Calculations of Energy Loss, Range, Pathlength, Staggling, Multiple Scattering, and the Probability of Inelastic Nuclear Collisions for 0.1- to 1000-MeV Protons, Technical Report No. AFWL-TR-65-150, Air Force Weapons Laboratory, Kirtland Air Force Base, New Mexico, 1966.

47. The scintillator telescopes used were the proton and deuteron detectors used to monitor target thickness (Sec. II.C.). The telescopes were repositioned and appropriate degrader was installed.

48. This was measured at a beam rate low enough that accidental coincidences were negligible.

49. A. M. Cormack, Nucl. Instr. and Methods 15, 268 (1962).

0 0 0 - 4 3 0 0 9 9 0

LEGAL NOTICE

This report was prepared as an account of work sponsored by the United States Government. Neither the United States nor the United States Energy Research and Development Administration, nor any of their employees, nor any of their contractors, subcontractors, or their employees, makes any warranty, express or implied, or assumes any legal liability or responsibility for the accuracy, completeness or usefulness of any information, apparatus, product or process disclosed, or represents that its use would not infringe privately owned rights.

TECHNICAL INFORMATION DIVISION
LAWRENCE BERKELEY LABORATORY
UNIVERSITY OF CALIFORNIA
BERKELEY, CALIFORNIA 94720